CrossMark

Trans-Neptunian Objects Found in the First Four Years of the Dark Energy Survey

Pedro H. Bernardinelli[1], Gary M. Bernstein[1], Masao Sako[1], Tongtian Liu[1], William R. Saunders[1,2], Tali Khain[3],
Hsing Wen Lin[3], David W. Gerdes[3,4], Dillon Brout[1], Fred C. Adams[3,4], Matthew Belyakov[1],
Aditya Inada Somasundaram[1], Lakshay Sharma[1], Jennifer Locke[1], Kyle Franson[3,5], Juliette C. Becker[4], Kevin Napier[3],
Larissa Markwardt[4], James Annis[6], T. M. C. Abbott[7], S. Avila[8], D. Brooks[9], D. L. Burke[10,11], A. Carnero Rosell[12,13],
M. Carrasco Kind[14,15], F. J. Castander[16,17], L. N. da Costa[13,18], J. De Vicente[12], S. Desai[19], H. T. Diehl[6], P. Doel[9], S. Everett[20],
B. Flaugher[6], J. García-Bellido[8], D. Gruen[10,11,21], R. A. Gruendl[14,15], J. Gschwend[13,18], G. Gutierrez[6], D. L. Hollowood[20],
D. J. James[22], M. W. G. Johnson[15], M. D. Johnson[15], E. Krause[23], N. Kuropatkin[6], M. A. G. Maia[13,18], M. March[1],
R. Miquel[24,25], F. Paz-Chinchón[14,15], A. A. Plazas[26], A. K. Romer[27], E. S. Rykoff[10,11], C. Sánchez[1], E. Sanchez[12],
V. Scarpine[6], S. Serrano[16,17], I. Sevilla-Noarbe[12], M. Smith[28], F. Sobreira[13,29], E. Suchyta[30], M. E. C. Swanson[15], G. Tarle[3],
A. R. Walker[7], W. Wester[6], and Y. Zhang[6]
(The DES Collaboration)

[1] Department of Physics and Astronomy, University of Pennsylvania, Philadelphia, PA 19104, USA; pedrobe@sas.upenn.edu
[2] Department of Astronomy, Boston University, Boston, MA 02215, USA
[3] Department of Physics, University of Michigan, Ann Arbor, MI 48109, USA
[4] Department of Astronomy, University of Michigan, Ann Arbor, MI 48109, USA
[5] Department of Astronomy, The University of Texas at Austin, Austin, TX 78712, USA
[6] Fermi National Accelerator Laboratory, P.O. Box 500, Batavia, IL 60510, USA
[7] Cerro Tololo Inter-American Observatory, National Optical-Infrared Astronomy Observatory, Casilla 603, La Serena, Chile
[8] Instituto de Fisica Teorica UAM/CSIC, Universidad Autonoma de Madrid, E-28049 Madrid, Spain
[9] Department of Physics & Astronomy, University College London, Gower Street, London WC1E 6BT, UK
[10] Kavli Institute for Particle Astrophysics & Cosmology, P.O. Box 2450, Stanford University, Stanford, CA 94305, USA
[11] SLAC National Accelerator Laboratory, Menlo Park, CA 94025, USA
[12] Centro de Investigaciones Energéticas, Medioambientales y Tecnológicas (CIEMAT), Madrid, Spain
[13] Laboratório Interinstitucional de e-Astronomia—LIneA, Rua Gal. José Cristino 77, Rio de Janeiro, RJ—20921-400, Brazil
[14] Department of Astronomy, University of Illinois at Urbana-Champaign, 1002 W. Green Street, Urbana, IL 61801, USA
[15] National Center for Supercomputing Applications, 1205 West Clark St., Urbana, IL 61801, USA
[16] Institut d'Estudis Espacials de Catalunya (IEEC), E-08034 Barcelona, Spain
[17] Institute of Space Sciences (ICE, CSIC), Campus UAB, Carrer de Can Magrans, s/n, E-08193 Barcelona, Spain
[18] Observatório Nacional, Rua Gal. José Cristino 77, Rio de Janeiro, RJ—20921-400, Brazil
[19] Department of Physics, IIT Hyderabad, Kandi, Telangana 502285, India
[20] Santa Cruz Institute for Particle Physics, Santa Cruz, CA 95064, USA
[21] Department of Physics, Stanford University, 382 Via Pueblo Mall, Stanford, CA 94305, USA
[22] Center for Astrophysics | Harvard & Smithsonian, 60 Garden Street, Cambridge, MA 02138, USA
[23] Department of Astronomy/Steward Observatory, University of Arizona, 933 North Cherry Avenue, Tucson, AZ 85721-0065, USA
[24] Institució Catalana de Recerca i Estudis Avançats, E-08010 Barcelona, Spain
[25] Institut de Física d'Altes Energies (IFAE), The Barcelona Institute of Science and Technology, Campus UAB, E-08193 Bellaterra (Barcelona), Spain
[26] Department of Astrophysical Sciences, Princeton University, Peyton Hall, Princeton, NJ 08544, USA
[27] Department of Physics and Astronomy, Pevensey Building, University of Sussex, Brighton BN1 9QH, UK
[28] School of Physics and Astronomy, University of Southampton, Southampton SO17 1BJ, UK
[29] Instituto de Física Gleb Wataghin, Universidade Estadual de Campinas, 13083-859, Campinas, SP, Brazil
[30] Computer Science and Mathematics Division, Oak Ridge National Laboratory, Oak Ridge, TN 37831, USA

Abstract

We present a catalog of 316 trans-Neptunian bodies (TNOs) detected from the first four seasons ("Y4" data) of the Dark Energy Survey (DES). The survey covers a contiguous 5000 deg^2 of the southern sky in the *grizY* optical/NIR filter set, with a typical TNO in this part of the sky being targeted by 25–30 Y4 exposures. This paper focuses on the methods used to detect these objects from the ≈60,000 Y4 exposures, a process made challenging by the absence of the few-hour repeat observations employed by TNO-optimized surveys. Newly developed techniques include: transient/moving object detection by comparison of single-epoch catalogs to catalogs of "stacked" images; quantified astrometric error from atmospheric turbulence; new software for detecting TNO linkages in a temporally sparse transient catalog, and for estimating the rate of spurious linkages; use of faint stars to determine the detection efficiency versus magnitude in all exposures. Final validation of the reality of linked orbits uses a new "sub-threshold confirmation" test, wherein we demand the object be detectable in a stack of the exposures in which the orbit indicates an object should be present, but was not individually detected. This catalog contains all validated TNOs which were detected on ⩾6 unique nights in the Y4 data, and is complete to $r \lesssim 23.3$ mag with virtually no dependence on orbital properties for bound TNOs at distance 30 au $< d <$ 2500 au. The catalog includes 245 discoveries by DES, 139 not previously published. The final DES TNO catalog is expected to yield >0.3 mag more depth, and arcs of >4 yr for nearly all detections.

Unified Astronomy Thesaurus concepts: Trans-Neptunian objects (1705); Orbit determination (1175); Astronomy data analysis (1858); Transient detection (1957)

Supporting material: FITS files

1. Introduction

Trans-Neptunian objects (TNOs) are probes of the dynamical and chemical history of the solar system. These planetesimals are relics of major dynamical events among and beyond the giant planets, with the current observed orbital distribution of the Kuiper Belt being a signature of large-scale changes in the positions of the giant planets (Fernández & Ip 1984; Malhotra 1993; Duncan et al. 1995; Hahn & Malhotra 2005; Tsiganis et al. 2005; Levison et al. 2008; Nesvorný 2015; Kaib & Sheppard 2016; Nesvorný & Vokrouhlický 2016). By constraining the detailed structure of the multiple populations in the distant solar system (see Gladman et al. 2008 for a review), one can further probe numerous dynamical processes, such as instabilities in Neptune's orbit (Dawson & Murray-Clay 2012), interactions between these planetesimals and Neptune (Gomes 2003; Morbidelli et al. 2008), the presence of distant planetary-mass perturbers (Trujillo & Sheppard 2014; Batygin & Brown 2016; Volk & Malhotra 2017), the effect of close stellar encounters (Jílková et al. 2015), the birth cluster of the solar system (Adams 2010; Brasser & Schwamb 2015), and perturbations from Galactic tides (Duncan et al. 2008; Bannister et al. 2017).

Searches for TNOs face a trade-off between depth and search area. As the resources available for TNO searches, quantified by the product of field of view (FOV) × (telescope area) × (observing time), have increased due to improved detector technology, the envelope of searches in the depth-area plane has expanded. Dedicated TNO surveys using large-format CCD cameras on 4 or 8 m class telescopes now cover hundreds to thousands of square degrees (Bannister et al. 2016, 2018; Weryk et al. 2016; Chen et al. 2018; Sheppard et al. 2019). The Dark Energy Survey (DES) was allocated 575 nights of time on the 4 m Blanco Telescope in Cerro Tololo over six seasons from 2013 to 2019, with the primary goals of characterizing the distribution of dark matter and the nature of the Hubble acceleration (The Dark Energy Survey Collaboration 2018a, 2018b, 2019a, 2019b, 2019c). The survey strategy is, nominally, to image the same contiguous 5000 deg^2 patch of high-Galactic-latitude southern sky in five optical/NIR bands each year. While not optimized for TNO discovery, the survey is nonetheless capable of pushing out the depth/area envelope of TNO searches, particularly for high-inclination TNOs. The Dark Energy Camera (DECam; Flaugher et al. 2015), with its 3 deg^2 field of view and 520 Mpix science array, is a powerful instrument for survey science. Among previous large-scale surveys optimized for TNO detection is the Deep Ecliptic Survey (Elliot et al. 2005). We caution the reader that, although the acronym DES is the same as our survey and both surveys made use of the Blanco telescope, there is no connection with the work presented herein. The Dark Energy Survey wide survey covers 10× more area with ≈1 mag deeper TNO detection threshold than the Deep Ecliptic Survey, using around five times more nights of 4 m time, a consequence of the higher quantum efficiency and larger FOV offered by DECam. Discoveries of individual objects of interest have been reported from the DES data (Gerdes et al. 2016, 2017; Becker et al. 2018; Khain et al. 2018; Lin et al. 2019) as well as from DECam observations allocated for directed TNO searches (Trujillo & Sheppard 2014; Sheppard et al. 2016, 2018; Sheppard & Trujillo 2016). Astrometric data from DES observations of known TNOs have been incorporated into forecasts of future occultation events by Banda-Huarca et al. (2019).

Here we provide the first comprehensive inventory of TNOs detected in the DES observations, from analysis of the first four seasons. We also describe the improvements that are expected when the full survey data are searched (the final observations were in 2019 January).

Surveys designed to detect TNOs almost invariably schedule pairs of observations of a sky region with time intervals that are at least an hour, but less than about a day, apart (e.g., Jewitt & Luu 1993; Allen et al. 2001; Trujillo et al. 2001; Bernstein et al. 2004; Elliot et al. 2005; Jones et al. 2006; Fraser et al. 2010; Schwamb et al. 2010; Petit et al. 2011; Rabinowitz et al. 2012; Alexandersen et al. 2016; Bannister et al. 2016; Sheppard et al. 2016; Weryk et al. 2016; Chen et al. 2018) (note that Tombaugh 1946 used a few-day interval). In this regime, the apparent motion of a TNO is large enough to be readily identified in ≈1″ seeing, but the motion is small enough ($\lesssim 1'$) that two detections of the same TNO are readily identified as such. The rate of such nearby pairs that are *not* TNOs is small (e.g., a single asteroid near turnaround, or coincident detections of two distinct asteroids). Most large-scale, small-body search algorithms rely on the initial identification of such pairs (e.g., Denneau et al. 2013; Holman et al. 2018).

The DES observing strategy specifically *avoids* repeat observations of the same filter/field combination on the same night, so that the variations in weather are spread across the survey footprint, and the final survey is more valuable if it is more homogeneous. There is, therefore, no useful way to distinguish TNOs from asteroids in the catalog of >20 million transient unresolved DES sources. In this paper, we define a *transient* to be a source that appears in the sky in a given location on only a single night, thus including both moving objects and (non-repeating) variable sources. We must, like Perdelwitz et al. (2018), devise algorithms for linking together those detections corresponding to the same TNO. The linking process, while harder than for a TNO-optimized survey, is fully feasible with proper use of spatial–temporal tree structures for the transients, e.g., as in Kubica et al. (2007). A high-efficiency and high-purity search of the DES data is possible because any given TNO is targeted nominally twice per filter per season. This highly redundant search, while not maximizing the number of TNO discoveries per observation, does mean that the DES cadence automatically yields high-quality orbits and multi-band magnitudes for nearly all detected TNOs.

Another difference between the DES survey and those designed for TNO detection is that most of the DES footprint is at high ecliptic latitudes (Figure 1). This will allow the DES to obtain stronger constraints on the high-inclination population.

Section 2 summarizes the observations and image processing procedures of DES, details the extraction of a catalog of transient sources from these data, and evaluates the detection thresholds in the individual exposures. Section 3 presents the algorithms used to identify TNOs from the catalog of single-epoch transients, including quantification of the rate of false-positive linkages. Section 4 defines the "sub-threshold significance" statistic: we examine images that cover the putative object's orbit, but did not yield a detection. A real object will be present but with signal lurking below detection threshold, while a spurious linkage will have zero signal
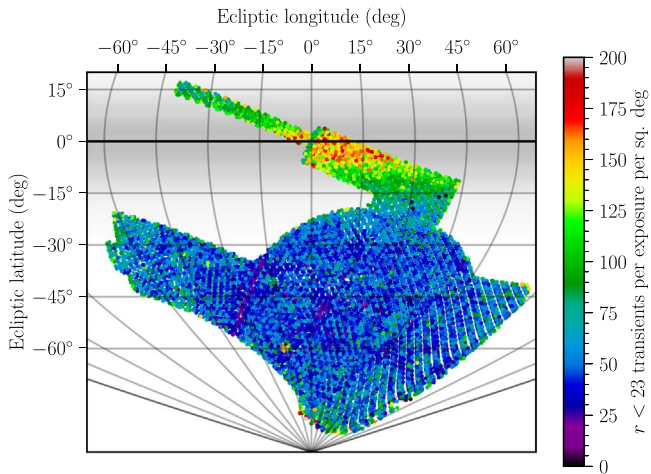
Figure 1. Sanson–Flamsteed equal-area projection of the transient map in ecliptic coordinates for the DES Y4 exposures, with the color of each *r*-band exposure denoting the sky density of transients on this exposure. We restrict transient counts to *r* < 23, where nearly all exposures are highly complete, so that this map reflects sky density variations rather than changes in the limiting magnitude of exposures. The density increases with ecliptic latitude, peaking at the ecliptic, being dominated by asteroids. The darker stripes running through the round central region are places where the tiling of the sphere requires us to overlap exposures more heavily. This leads to deeper coadd images and more effective rejection of spurious transients. The shaded gray region represents the latitudinal density of the asteroid belt.

on these unlinked images. Section 5 evaluates the effectiveness of the search through insertion of synthetic TNOs into the transient catalog. The catalog of secure Y4 DES TNO detections is presented in Section 6. In Section 7, we summarize and highlight the improvements to be expected from next DES TNO catalog release. This will make use of the full DES observation set, yielding improved depth and orbital parameters, but will also gain depth from several methodological upgrades. This paper will describe only the production of the Y4 DES TNO catalog; analysis of its contents will be described in further publications. While we describe here the methods that are used to determine the survey's sensitivity versus TNO magnitude and orbital parameters, we will defer the full-scale application of these methods until the analysis of the final DES TNO catalog. Thus we do not anticipate production or publication of the detailed completeness functions or a survey simulator for the catalog presented herein.

For readers who are more interested in the catalog than in the details of the methods used to discover its contents, we would suggest skimming Section 2 and then skipping to Section 5 to see the nature of the final selection function, and later sections with the contents of the catalog.

The DES collaboration has experimented with methods for identifying and linking transients that differ from those presented in this paper. Many TNOs have been discovered or measured (Gerdes et al. 2016, 2017; Becker et al. 2018; Khain et al. 2018, 2020; Lin et al. 2019) using difference imaging for transient identification (Kessler et al. 2015). The search described in this paper is the first to search the full Y4 survey in a uniform fashion. For reference, we include in this paper a table of objects that were discovered in DES data by the other methods, but missed in this Y4 search. As will be discussed in Section 6, all such cases are found to be TNOs that lie outside

the selection criteria of the Y4 search, i.e., the Y4 search is seen to be complete within its stated criteria.

2. The Transient Catalog

2.1. Observations

The DES observational strategy is fully described in Diehl et al. (2016, 2018) but we summarize the relevant details here. The "wide" portion of the survey aims to completely tile the 5000 deg^2 footprint with 10 × 90 s exposures in each of the *g*, *r*, *i*, and *z* bands, and 6 × 45 + 2 × 90 s in the *Y* band, such that the completed wide survey will comprise ≈80,000 DECam exposures. DES observations are taken in seasons beginning in August and ending in February each year. The wide survey exposures are interleaved with a "deep" survey which images 10 DECam pointings (≈30 deg^2) at ≈ weekly intervals in the *griz* bands, primarily for detection and measurement of high-redshift Type Ia supernovae (Bernstein et al. 2012). The Y4 TNO search reported herein was conducted only on the wide-survey images, but we have also searched much of the deep data and reported TNO detections to the Minor Planet Center (MPC) (Gerdes et al. 2016, 2017; Becker et al. 2018; Khain et al. 2018, 2020; Lin et al. 2019).

Observations are scheduled with the OBSTAC algorithm (Neilsen & Annis 2013), which works to optimize the quality and homogeneity of the final wide-survey products in the face of variable clouds, seeing, and moonlight, while balancing the needs of the deep survey for temporally regular sampling. Importantly, part of this optimization is to avoid imaging the same part of the wide survey more than once in any filter on any single night (the goal is to spread the weather fluctuations across the footprint to homogenize the final survey products). Occasionally OBSTAC will elect to take successive exposures at the same pointing in two different filters, typically *g*, *r*, and/or *i* in dark time and *zY* in bright conditions. These pairs, with only two minute intervals between them, are not useful for detecting TNO motion. Repeat imaging on any time interval longer than two minutes and shorter than one day is very rare. When we calculate the robustness of our TNO detections against false-positive linkages, we will always consider multiple detections on the same night to be fully correlated (not independent) since most sources of false positives (asteroids, variable stars, artifacts from bright sources) will tend to repeat in successive exposures. Each DES exposure is processed and evaluated the next day. Exposures failing to meet minimum standards for seeing and signal-to-noise ratio (S/N) are discarded, and their pointings placed back on the queue. We do not search rejected images for TNOs.

Nominally the survey goals were to cover half of the footprint with four "tilings" per filter in the first year, cover the other half with four tilings in the second year, and then two full tilings per year for three succeeding years. Variability in weather and availability of fields meant that this plan is only a rough approximation to reality. In particular, very poor weather in year 3 put the survey behind schedule, and an additional half-season's worth of observations were allocated for a sixth year to complete the survey. In the Y4 data under analysis here, a typical point in the footprint has been within the DECam field of view for around seven exposures per band. Within the field of view, 15%–20% of the sky is lost to gaps between the DECam CCDs, regions of defective CCDs, and area lost in the

glare of bright sources. Thus a typical TNO will be cleanly imaged $\approx 6\times$ per filter in the Y4 data.

One other observational detail of note is that DECam has a two-blade shutter which takes ≈ 1 s to sweep across the focal plane (Flaugher et al. 2015, Section 6.1). Successive exposures sweep the blades in opposite directions. We assign all TNO detections to a time corresponding to the midpoint of the shutter-open interval in the center of the focal plane. The true mean time of the open-shutter interval for any particular TNO's exposure may differ by up to ≈ 0.5 s in an unknown direction. Since the TNO apparent motion in this time interval is <1 mas, the shutter uncertainty contributes negligibly to errors in orbit determination.

2.2. Processing and Cataloging

For the analysis presented here, we make use of two distinct types of object catalogs produced during standard DES processing (Morganson et al. 2018): the single-epoch (SE) produced for each individual exposure, and the multi-epoch (a. k.a. "coadd") catalogs produced from an image averaging all exposures.

The SE catalogs used for this search come from the "Final Cut" reduction of the internal "Y4A1" data release. This processing includes the detrending and calibration of the raw CCD data. Artifacts such as saturated pixels close to bright stars, cosmic rays, and streaks are masked, sky background template images are subtracted from the science image, and the point-spread function (PSF) is modeled via the bright stars. Sources are detected in the images using SEXTRACTOR (Bertin & Arnouts 1996), with its default 3×3 pixel filter first being applied to the image. The detection criteria are that a source needs 6 pixels (DETECT_MINAREA = 6) above the detection threshold DETECT_THRESH = ANALYSIS_THRESH = 1.5. A variety of position, flux, and shape measurements are made on each object and recorded in the output SE catalog.

The coadd catalogs in use here come from an internal data release labeled "Y3A2," i.e., they combine images only from the first three DES seasons. Sources are detected on a sum of all the r, i, and z images using SEXTRACTOR settings similar to the SE values above. The coadd catalogs and images used in this work are the same as those in the public DR1 release[31] (Abbott et al. 2018).

2.3. Calibration

The DES catalogs are exquisitely well calibrated to a common photometric system across the focal plane (Bernstein et al. 2017a) and across all the exposures of the survey (Burke et al. 2017). Comparison of DES magnitudes to *Gaia* DR2 magnitudes show uniformity across the footprint to ≈ 6 mmag rms (Abbott et al. 2018, Section 4.2). Trailing of TNO images in the 90 s DES wide exposures has negligible impact on photometry: at the maximal rate of apparent motion for objects $\geqslant 30$ au of $5''$ hr^{-1}, the object would move $0\rlap{.}''12$. The second moment of the trail is then <1% of the second moment of the PSF, and the point-source calibrations should be accurate to <0.01 mag even for this maximal apparent motion.

Every DES exposure has an astrometric map from pixel coordinates to the *Gaia* DR1 (Lindegren et al. 2016; Brown et al. 2016) celestial reference frame. Here again we benefit

from extensive DES calibration efforts. Bernstein et al. (2017b) describes the DECam astrometric model, demonstrating that all distortions induced by the telescope, instrument, and detectors are known to 3–6 mas rms. We apply this model to all exposures in the Y4 DES TNO search. The astrometric uncertainties for bright TNO detections are dominated by stochastic displacements caused by atmospheric turbulence, at 10–15 mas rms on typical exposures. Below we describe the estimation of this turbulence uncertainty for each exposure. Fainter detections' astrometric uncertainties are dominated by shot noise in the centroiding of the image.

The astrometric solution includes terms for differential chromatic refraction (DCR) in the atmosphere and lateral color in the optics, which are calibrated in terms of the $g - i$ color of the source. Similarly the photometric solution includes color terms. The maximal amplitude of the DCR (for airmass $X < 2$) and lateral color are ≈ 80 and 40 mas per mag of $g - i$ color, respectively, for g-band observations, and five or more times smaller in other bands (Bernstein et al. 2017b). The $g - i$ colors of all stars are measured directly by the DES, which fixes the reference frame, but the TNO apparent position will depend on its (unknown) color. Our TNO search is executed using positions that assume a nominal color, $g - i = 0.61$ (a typical stellar color). Only after a TNO is linked can we estimate its color. The final positions, magnitudes, and orbital parameters reported herein are calculated after refinement using the proper chromatic corrections.

The procedure for estimating the atmospheric turbulence contribution to astrometric errors is as follows.

  i. For each high-S/N star i in the survey footprint, we calculate a mean position by averaging the positions predicted by the astrometric model in all DES exposures, as well as any position available in *Gaia* DR1, to produce a "truth" value $\bar{x}_i$.
  ii. Restricting ourselves to the positions x_i measured on an individual DES exposure, we find the measurement error $\Delta x_i \equiv x_i - \bar{x}_i = (\Delta x_i, \Delta y_i)$ from the mean position. The displacement is measured in a local gnomonic projection, with x pointing to local equatorial east and y north.
  iii. A cubic polynomial function of field coordinates is fit to the Δx_i and adopted as the large-scale distortions from atmospheric and turbulent refraction for this exposure. This fit is subtracted from the Δx_i.
  iv. We calculate the two-point correlation functions of astrometric error, averaging over all pairs of stars in the exposure versus their separation r:

$$\xi_x(r) = \langle \Delta x_i \Delta x_j \rangle_{|x_i - x_j| = r}, \tag{1a}$$

$$\xi_y(r) = \langle \Delta y_i \Delta y_j \rangle_{|x_i - x_j| = r}, \tag{1b}$$

$$\xi_\times(r) = \langle \Delta x_i \Delta y_j \rangle_{|x_i - x_j| = r}. \tag{1c}$$

An example of the behavior of ξ is shown in Figure 2.
  v. We assign a 2D Gaussian positional uncertainty to each detection in the exposure, with a covariance matrix given by

$$\Sigma_{\rm atm} = \begin{pmatrix} \langle \xi_x \rangle & \langle \xi_\times \rangle \\ \langle \xi_\times \rangle & \langle \xi_y \rangle \end{pmatrix} \tag{2}$$

where the ξ values are averaged over the separation range $24'' < r < 40''$ where they typically plateau. Note that this use of the correlation function at $r > 0$ removes any
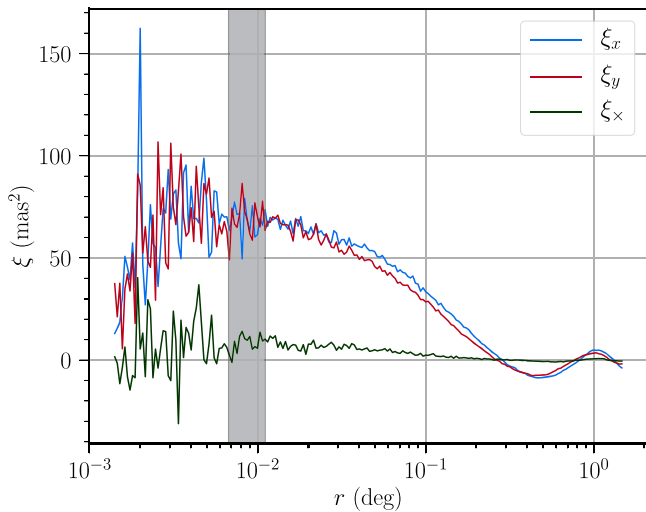
Figure 2. Correlation function $\xi(r)$ of astrometric errors for high-S/N stars separated by angle r. This plot gives the average of $\xi(r)$ for all g-band exposures in a small region of the survey, taken across 4 yr of observations. The shaded region denotes where the ξ values are averaged to establish the covariance matrix of atmospheric turbulence.
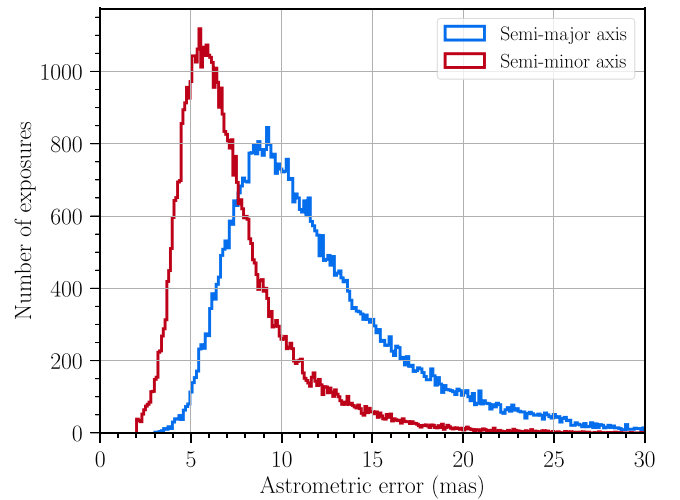

Figure 3. Distribution of the semimajor and semiminor axes for the atmospheric turbulence error ellipses for all exposures used in the DES internally released "Y4A1" catalog.

contribution due to shot noise of individual stellar measurements.

Figure 3 shows the histogram of atmospheric turbulence strength in the exposures. The typical atmospheric turbulence is seen to be ≈ 10 mas. The astrometric errors are typically substantially anisotropic on most individual exposures, with $\Sigma_{xx} \neq \Sigma_{yy}$ and $\Sigma_{xy} \neq 0$, because astrometric errors are substantially different parallel versus perpendicular to the prevailing wind direction.

The final astrometric uncertainty assigned to each transient is the quadrature sum of the atmospheric turbulence ellipse in Equation (2) with the circularly symmetric shot noise error in the centroid reported by SEXTRACTOR.

2.4. Identifying Single-night Transients

The computational burden of linking TNOs from the transient catalog scales roughly as n^3, where n is the density of transient detections per square degree per exposure. It is therefore of great importance to minimize n while retaining all true TNO detections in the transient catalog. Because asteroids are indistinguishable from TNOs at the single-exposure level, the transient catalog must include all detected asteroids, which will greatly outnumber the TNOs.[32] Asteroids thus form an irreducible source of false-positive TNO transient detections, and our goal, therefore, is to reduce any other spurious transient detections to a level well below the asteroid density.

We wish to identify all sources in the thousands of DES images that are present in a given sky location for only a single night. We begin by matching the SE in all bands and coadd catalogs (in which each detection has information from all bands) by sky coordinates. All detections in a small region are projected into a tangent plane and then grouped with a kD-tree (Maneewongvatana & Mount 1999) friends-of-friends (FoF) algorithm that links detections within 0″.5 of each other.

For each group of SE detections, we calculate the following quantities:

1. whether or not it is matched to a coadd detection, COADD = 1, 0;
2. how far apart in time are the first and the last SE detections of the match group, $\Delta t \equiv t_{\text{last}} - t_{\text{first}}$;
3. how much fainter or brighter the SE detection is compared to the coadd detection in the same band (when present), $\Delta m \equiv m_{\text{SE}} - m_{\text{coadd}}$.

If the SE detection is a detection of a solar system object, we do not expect any flux to be present at this location on the other exposures contributing to the coadd taken more than a few hours away from the SE detection. If there are K exposures in the coadd, then the averaging process will reduce the apparent flux of the source in the coadd by a factor $1/K$, leaving the coadd source with a magnitude fainter than the SE value by $2.5 \log_{10} K \geqslant 0.75$ mag for $K \geqslant 2$. The coadd source should thus either be absent or significantly fainter than the SE source. We therefore implement the following cut to retain potential solar system measurements while eliminating many variable fixed (stellar) sources:

1. COADD = 1, $\Delta t < 2$ days, $\Delta m \leqslant -0.4$; OR
2. COADD = 0, $\Delta t < 2$ days.

Note that $\Delta t < 2$ days is by itself an insufficient condition, since it would include many faint sources that are pushed above detection thresholds on only 1–2 exposures because of intrinsic variability or noise fluctuations. The veto by the more sensitive coadd images solves this issue, with the $\Delta m \leqslant -0.4$ threshold estimated empirically to include nearly all truly moving sources (TNOs), as illustrated in Figure 4.

Unlike Goldstein et al. (2015) or Lin et al. (2018), we do not make cuts on object sizes or other morphological features of detections, as these measures are too noisy to be useful discriminants of non-stellar artifacts from TNOs for sources at the threshold of detectability. We are willing to accept higher false-positive rates in order to keep the lowest flux threshold for true TNOs.

The first panel of Figure 5 maps the sky locations of transient detections, revealing many coherent structures that cannot be produced by TNOs, asteroids, or other true celestial moving objects. These structures correspond to image artifacts that were not successfully masked by the SE pipeline, such as

---

[32] Previously known asteroids could be deleted from the transient catalog, but at these magnitudes only a small fraction of asteroids are currently cataloged.
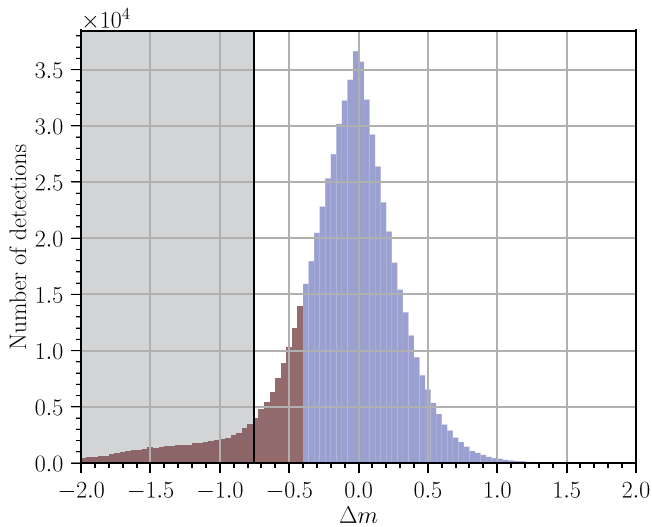
Figure 4. Distribution of Δm, the difference in magnitude between single-night detections and the magnitude of the matched object in the coadd frame, shown for detections in 25deg^2 of the survey. We posit this to be the sum of a population with symmetric distribution about $\Delta m = 0$ caused by noise and variability of static sources, plus a tail of highly negative Δm values containing moving objects (peaking at $\Delta m \approx -1.5$). True single-night transients are expected to have, on average, $\Delta m < -0.75$ (shaded region), because the single-night flux will be reduced by the number of (zero-flux) other exposures' data averaged together. All objects in the red region at $\Delta m < -0.4$ are included in the transient catalog, with this cut selected to give us a high probability of capturing all of the true single-night transients.
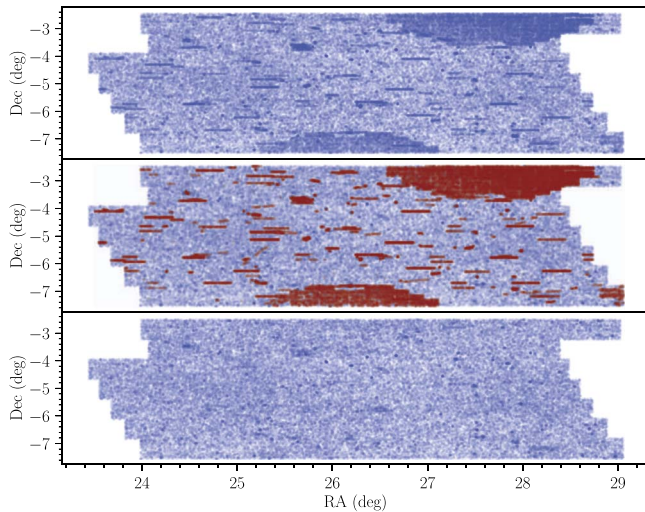
Figure 5. Three stages of the transient catalog. From top to bottom: (1) the catalog before the cleaning process; (2) identification of the coherent structures; (3) coherent structures removed, showing the output catalog. Note that there are still some coherent structures remaining, but these are now a small minority of the total transient catalog.

meteor/satellite/airplane streaks, bad pixel columns, and artifacts from detections around bright sources. There are also some exposures with incorrect astrometric solutions, creating large numbers of spurious sources which do not match sky coordinates of other exposures' detections. We find empirically that the following steps applied to each exposure serve to reduce the number of spurious transient detections to level comparable to or below the irreducible asteroid density.

    i. The detections are clustered with FoF linking length of 60″.

    ii. Groups with more than 20 detections are removed from the catalog, as these correspond to entire CCDs or even exposures being identified as transient sources.

    iii. Groups that have between 10 and 20 detections could come from either accidental matching of true transients, or from coherent structures like unmasked streaks or arcs around bright stars.

    iv. To remove the latter, we test for a tendency of the points to lie along a line or curve: we evaluate the "bend angle," that is, the angle between the lines connecting each detection on this group to its two nearest neighbors. These angles are clipped to the range 0°–90°. If the average angle of all detections in the cluster is less than 15°, these detections are also removed from the catalog;

    v. We also remove transients within 30 pixels of any edge of a CCD, since source images cut off at CCD edges have mis-measured centroids that cause spurious mis-matches with their corresponding coadd sources.

Figure 6 illustrates the three cases described here. The second panel of Figure 5 shows the identified structures in a region of the survey, and the last panel shows the output, and final, transient catalog. Some spurious structures remain, but since the number of these is now well below the number of asteroids, there is little to be gained by further cuts on the transient catalog.

There are $\approx 7 \times 10^9$ SE detections in the 60,000 Y4 exposures. Of these, 2×10^7 are designated as transients (see Table 1).

2.5. Transient Density

Figure 1 presents a map of the density of bright ($r < 23$) transients for each DES Y4 r band exposure. At these magnitudes, most exposures are virtually complete (that is, the magnitudes of 50% completeness of each exposure is on average larger than this limit; see Section 2.6 for a discussion on the completeness estimates), and the drop in density from exposures with ~ 200 transients deg^{-2} close to the ecliptic plane to < 100 transients deg^{-2} far from it suggests that asteroids are comparable in the catalog to other astrophysical transients and artifacts.

This density is consistent with the sky density of 210 asteroids deg^{-2} brighter than $m_R = 23$ reported by SKADS (Gladman et al. 2009) for observations within a few degrees of opposition. DES may encounter fewer objects given that observations are not typically at opposition. We note that this density is consistent with the latitudinal asteroid density, computed from transforming the inclination distribution for all asteroids in the MPC[33] to an ecliptic latitudinal distribution following Brown (2001), plus a background level of 45 transients deg^{-2} independent of ecliptic latitude, as presented in the lower left panel of Figure 7.

We do not investigate the source of this background. They are not supernovae: from simulations of DES supernovae transient detections (Kessler et al. 2019), using supernovae rates from Jones et al. (2018), we expect only order unity supernovae (Ia and core collapse) per exposure to have $r < 23$, and yet they appear in only one night's exposure.

The upper right-hand panel of Figure 7 shows the average transient density in all exposures for all transients and, while

---

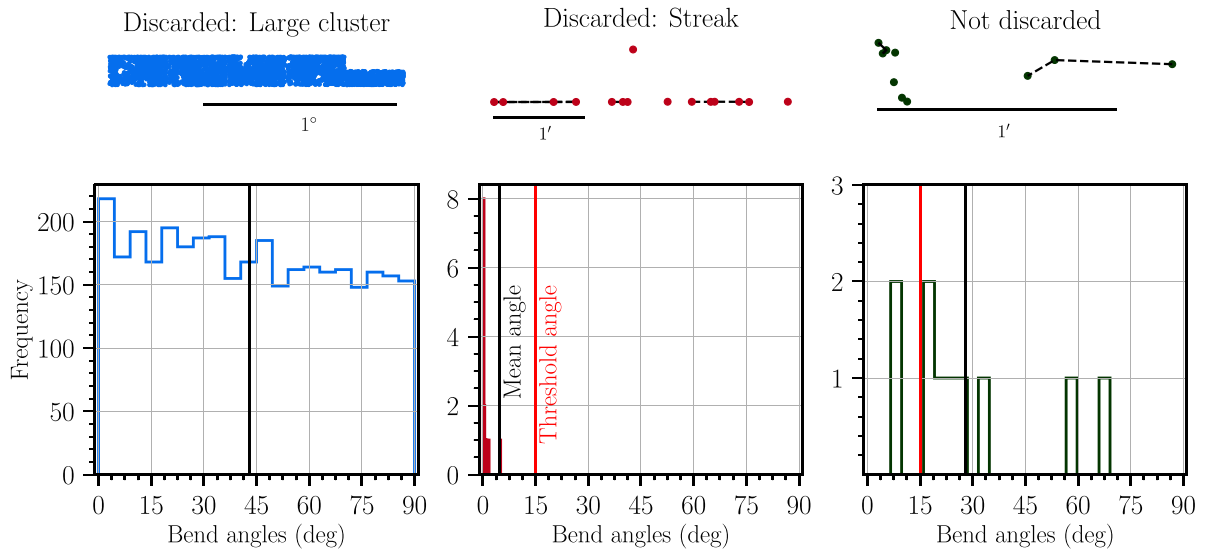[33] https://www.minorplanetcenter.net

Figure 6. Bend angle and clustering evaluation. First column: the transients from an exposure with astrometric misalignment (top), showing randomly distributed bend angles (bottom). Second column: a streak (with one spurious match) identified in the cleaning process (top), and the bend angle histogram (bottom) showing values close to zero. Third column: a randomly matched group (top), with no tendency in the bend angle histogram (bottom). In the last two scatter plots, the black dashed lines show some of the connected nearest neighbors, which define (visually) the bend angle.

Table 1
Overview of the Methodology, Showing in Italics the Steps That Transform the Initial Single-epoch Detection Catalogs through Intermediate Steps to a Verified TNO Catalog

Catalog/*Processing Step*	No. of Real Elements	No. of Injected Elements
Single epoch detections	7×10^9	⋯
→*Transient identification (Section 2)*→		
→*Blinded fake injection (Section 5.2)* →		
Transients	2×10^7	3.7×10^4
→*Pair finding (Section 3.1)*→		
Pairs	10^{12}	⋯
→*Triplet finding (Section 3.2)*→		
Triplets	6×10^{10}	⋯
→*Orbit growing (Section 3.3)*→		
→*Fake unblinding (Section 5.2)* →		
Sixlets	1684	2252
→*Reliability cuts (Section 3.4)*→		
Candidates	424	1727
→*Sub-threshold significance test (Section 4)*→		
Confirmed objects	316	⋯

Note. The last two columns show the number of objects at each stage and, where appropriate, the number of artificial objects that we have injected to test the pipeline efficiency.

the lower density far from the ecliptic is still present in the *griz* bands, the density plateaus at ∼200 per square degree per exposure (*r* band), defining the minimum false-positive rate for our search. The plateau at ∼150 transients deg^{-2} on the faint end corresponds to astrophysical transients (for example, stellar outbursts and supernovae that passed the Δt cut, as well as high-inclination asteroids), faint sources detected only once that passed the Δm cut, as well as image artifacts (e.g., cosmic rays, unmasked streaks). Image inspection on a randomly selected subset of false positives (identified in false TNO

linkages; see Section 4) indicates that most of the background comes from unmasked image artifacts. While the single-night transient catalog is not pure, the level of false positives is low enough that the search is feasible.

2.6. Detection Efficiency

To characterize the detection efficiency for point sources in a given exposure, we search the coadd catalogs for unresolved sources overlapping the exposure's footprint. Here, unresolved sources are defined as those with |SPREAD_MODEL_I| < 0.003 (see Section 8.1 of Drlica-Wagner et al. 2018). We then note each coadd source's magnitude in the band of the exposure, and record whether the source was detected in the SE processing of that exposure. This yields a list $m_{\mathrm{det},i}$ of the "true" (coadd) magnitudes of SE-detected point sources and another list $m_{\mathrm{non},j}$ of non-detected point sources in the exposure. If we posit a probability of detection $p(m)$ for this exposure, then the total probability of the observed outcome is

$$p_{\mathrm{tot}} = \prod_i p(m_{\mathrm{det},i}) \prod_j [1 - p(m_{\mathrm{non},j})]. \quad (3)$$

We posit that the completeness function for the exposure takes the form of a logit function

$$p(m) = \frac{c}{1 + \exp(k(m - m_{50}))}, \quad (4)$$

and we adjust the parameters m_{50}, c, and k to maximize p_{tot}. These then define the completeness function we adopt for this exposure. Figure 8 shows the distribution of m_{50} values for the exposures included in the Y4 wide-survey TNO search, as well as an example of the fit in one exposure.

3. Linking TNO Detections in the Transient Catalog

We work in a modified version of the Bernstein & Khushalani (2000, hereafter BK) formalism, which we present briefly here. All sky coordinates and state vectors are given in the ICRS, with origin at the solar system barycenter as
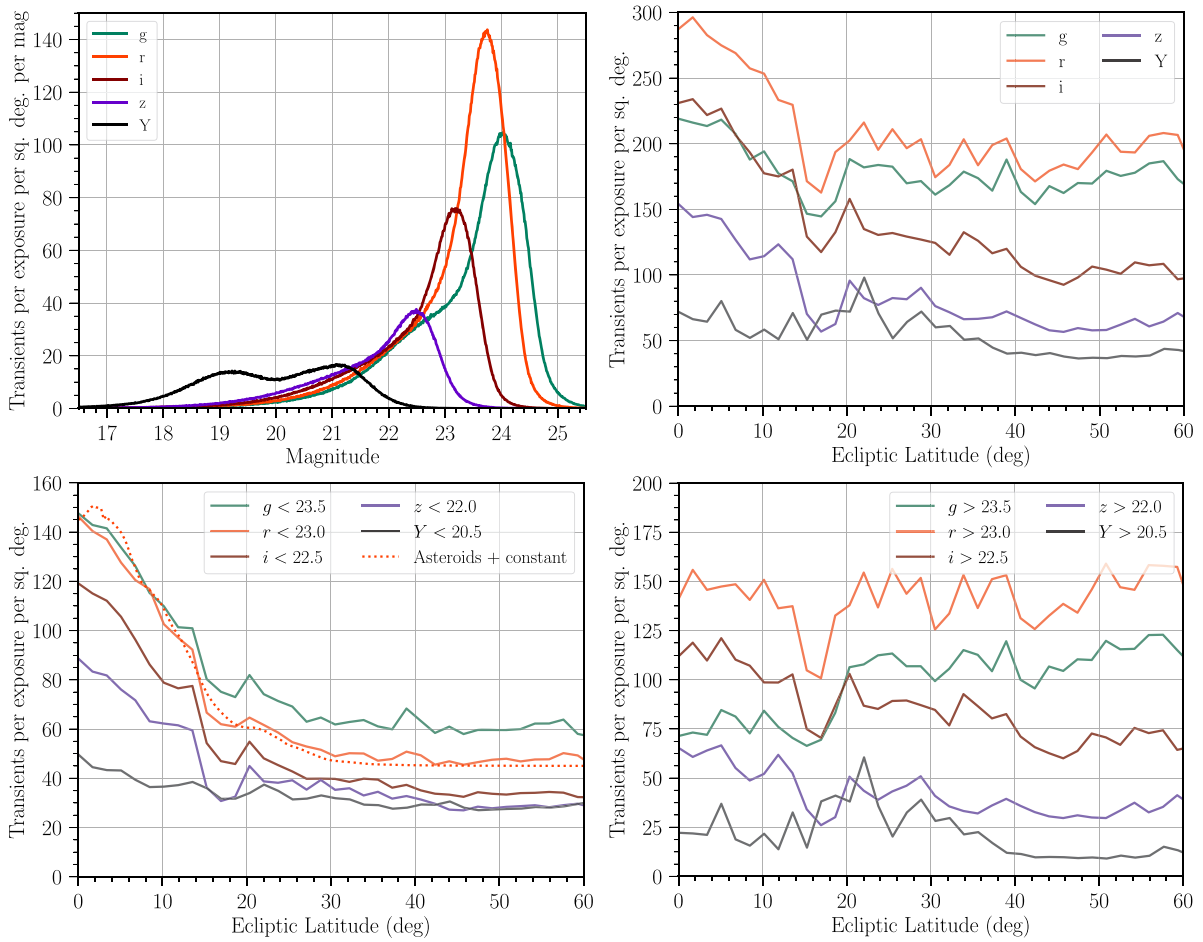
Figure 7. Upper left: histogram of magnitudes for all 22 million DES Y4 transients. Upper right: average transient density as a function of ecliptic latitude for all exposures. Lower left: bright (i.e., on the limit where most exposures are complete) transient density as a function of ecliptic latitude (similar to Figure 1). The orange dotted curve corresponds to the latitudinal density of the asteroid belt plus a background level. Lower right: faint transient density as a function of ecliptic latitude.
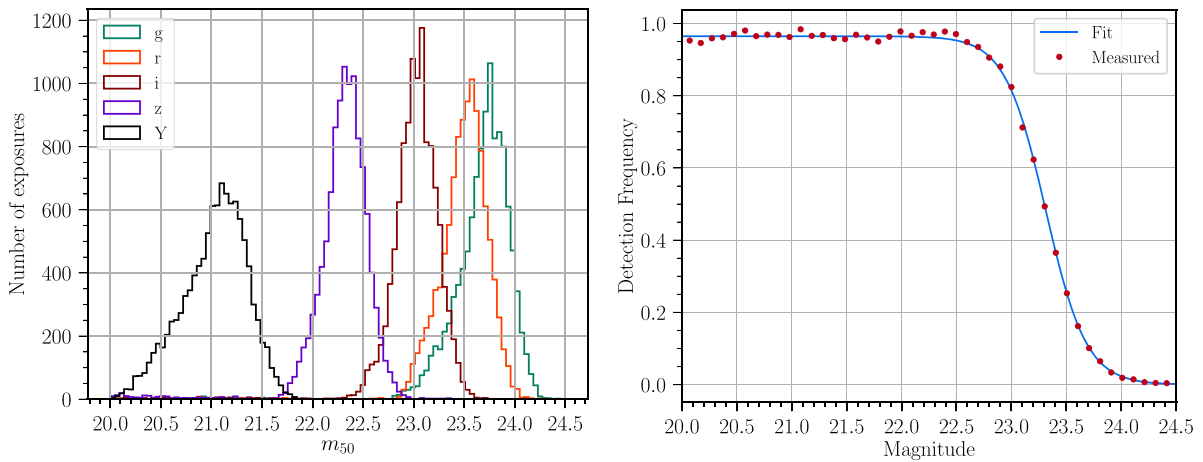

Figure 8. Left: histogram of the magnitude of 50% completeness, m_{50}, per band of the exposures used in the DES Y4 TNO search, as defined in Section 2.6. Right: example of the logit fit for an i band exposure. The measured parameters are $(m_{50}, c, k) = (23.31, 0.96, 5.40)$.

tabulated by the JPL Horizons ephemerides.[34] Barycentric orbital elements are calculated from state vectors using the total mass of the Sun plus all eight planetary systems as a central mass. During orbit fitting, gravitational accelerations are calculated using five gravitating masses: one at the location

of the Sun (with the mass of the terrestrial planets included), and one at each of the giant-planet barycenters, using the DE-430 ephemerides.

Observed angular positions (R.A. and decl.) are projected to the gnomonic coordinates (θ_x, θ_y) for the active patch (see BK for the proper transformation equations). The angular location of an orbit with phase space vector $\boldsymbol{P} = \{x_0, y_0, z_0, \dot{x}_0, \dot{y}_0, \dot{z}_0\}$

---

[34] http://ssd.jpl.nasa.gov

at time t_0 is written

$$\theta_x(t) = \frac{\alpha + \dot{\alpha}(t - t_0) + \gamma g_x(t) - \gamma x_{\mathrm{E}}(t)}{1 + \dot{\gamma}(t - t_0) + \gamma g_z(t) - \gamma z_{\mathrm{E}}(t)}, \quad (5a)$$

$$\theta_y(t) = \frac{\beta + \dot{\beta}(t - t_0) + \gamma g_y(t) - \gamma y_{\mathrm{E}}(t)}{1 + \dot{\gamma}(t - t_0) + \gamma g_z(t) - \gamma z_{\mathrm{E}}(t)}. \quad (5b)$$

Here, $\boldsymbol{x}_{\mathrm{E}} = (x_{\mathrm{E}}, y_{\mathrm{E}}, z_{\mathrm{E}})$ is the location of the observatory in a barycentric reference frame relative to the origin $\boldsymbol{x}_0$. $\boldsymbol{g} = (g_x, g_y, g_z)$ is the gravitational perturbation, defined by

$$\boldsymbol{g}(t_0) = \dot{\boldsymbol{g}}(t_0) = 0, \quad (6a)$$

$$\ddot{\boldsymbol{g}}(t) = -\sum_i GM_i \frac{\boldsymbol{x}(t) - \boldsymbol{x}_i(t)}{|\boldsymbol{x}(t) - \boldsymbol{x}_i(t)|^3}, \quad (6b)$$

where sum is done over the other bodies in the solar system, and

$$\alpha \equiv \frac{x_0}{z_0}, \quad \beta \equiv \frac{y_0}{z_0}, \quad \gamma \equiv \frac{1}{z_0}, \quad (7a)$$

$$\dot{\alpha} \equiv \frac{\dot{x}_0}{z_0}, \quad \dot{\beta} \equiv \frac{\dot{y}_0}{z_0}, \quad \dot{\gamma} \equiv \frac{\dot{z}_0}{z_0}. \quad (7b)$$

In this basis, the kinetic energy of a bound orbit is limited by

$$\dot{\alpha}^2 + \dot{\beta}^2 + \dot{\gamma}^2 \leqslant 2GM_\odot \gamma^3. \quad (8)$$

Here, we use the solar mass instead of the mass used to determine the barycenter as, for our purposes, the distinction is insignificant.

The recovery of TNOs from the full transient catalog proceeds by covering the full DES footprint with overlapping circular "patches" of radius 3°.5 having centers (R.A.$_i$, decl.$_i$). We also divide the full search range of heliocentric distances $30 < d < 2500$ au into bins of inverse distance $\gamma \equiv 1/d$ such that $\gamma_j - \delta\gamma_j \leqslant \gamma \leqslant \gamma_j + \delta\gamma_j$. The search proceeds as follows.

1. For each patch i:
   1. Define a gnomonic projection of sky coordinates about the pole (R.A.$_i$, decl.$_i$), to coordinates $\boldsymbol{\theta} = (\theta_x, \theta_y)$ with axes directed to ecliptic east and north, respectively.
   2. For each distance bin j:
      1. For each DES observing season $k = 1, 2, 3, 4$:
         1. Define a reference time t_0 at the midpoint of the observing season, and define an inertial Cartesian reference system with the x and y axes parallel to the θ_x, θ_y directions, and coordinate origin $\boldsymbol{x}_0$ at the location of the observatory at t_0.
         2. Identify all pairs of transients within 90 days of each other in season k which are compatible with a common bound orbit in distance bin j and with observed position at time t_0 lying within patch i.
         3. For each pair, identify all transients within an additional 90 days of the later member that form a triplet compatible with a bound TNO orbit within the distance bin.
         4. "Grow" each triplet into candidate n-lets by iterating the following process: fit an orbit to the n associated transients, using a prior that favors bound orbits within the distance bin (Equations (14) and (15)). Then find all potential additional transients (in any season) whose position is consistent with the fitted orbit. Each such

transient spawns a new $(n + 1)$-let. Multiple output orbits can result from a single triplet. Discard any n-let whose transients are a subset of another n-let, or whose transients fall on $N_{\mathrm{unique}} < 5$ distinct observing nights.
   3. Merge all of the candidate TNO n-lets from this patch by first re-fitting the orbit with the distance priors removed, then "growing" to incorporate any additional transients that fit the orbit, and then removing any that duplicate or are subsets of other n-lets. Each is now a candidate TNO orbit, and cuts are applied as described below to guard against false-positive linkages.
2. Merge the detections from all patches by removing duplicates.

These steps are described in more detail below. Note no requirements are placed on magnitude agreement when linking transients, since (a) the majority of transients will be near the detection thresholds, and such a cut will not be very effective, (b) we do not want to exclude TNOs with high-amplitude light curves, and (c) our search is conducted in multiple filters, and we do not want to bias our detections to particular colors of TNOs by demanding a particular difference between magnitudes in distinct bands.

3.1. Finding Pairs

For short arcs of distant objects, we can neglect the gravitational perturbation, and the effect of $\dot{\gamma}$ on observed position is highly suppressed. Rewriting Equations 5(a) and (b) with g, $\dot{\gamma} = 0$,

$$\alpha + \dot{\alpha}(t - t_0) = (1 - \gamma z_{\mathrm{E}})\theta_x + \gamma x_{\mathrm{E}}, \quad (9a)$$

$$\beta + \dot{\beta}(t - t_0) = (1 - \gamma z_{\mathrm{E}})\theta_y + \gamma y_{\mathrm{E}}. \quad (9b)$$

If we assume a distance $d = 1/\gamma$, this allows transformation of the (θ_x, θ_y) coordinates into an (α, β) system where the motion is linear. Holman et al. (2018) exploit this result for linking of tracklets, but we must link individual detections. From Equation (8), it becomes clear that after a time Δt an object in a bound orbit will be in a circle in the (α, β) plane of radius

$$r_2(\gamma, \Delta t) = \sqrt{2GM_\odot \gamma^3} \, \Delta t \quad (10)$$

centered around the first detection.

We start by selecting all exposures from season k which could potentially contain a TNO with γ within the selected bin and (α, β) within the 3°.5 patch radius. We apply the transformations from Equations 9(a) and (b) for γ_j to all transients detected in each exposure, and each set of resulting positions is used to constructed a kD tree. Trees for exposure pairs that are up to 90 days apart from each other are then searched for pairs of detections with a search radius as defined in Equation (10). This process is repeated at the edges of the distance bin ($\gamma_j \pm \delta\gamma_j$), resulting in the final list of pairs for the bin j.

The expected number of pairs of unassociated transients grows with the area of the search circles and the time interval between pairs. The mean number of such false-positive pairs between an exposure μ and all later exposures ν is

$$N_{2,\mu}(\gamma) = \sum_{\nu > \mu} 2\pi GM_\odot \gamma^3 \Delta t_{\mu\nu}^2 n_\mu n_\nu A_{\mathrm{DECam}} \quad (11)$$

where n_μ is the sky density of transients in exposure μ, $\Delta t_{\mu\nu}$ is the time interval between these two, and A_{DECam} is the imaging
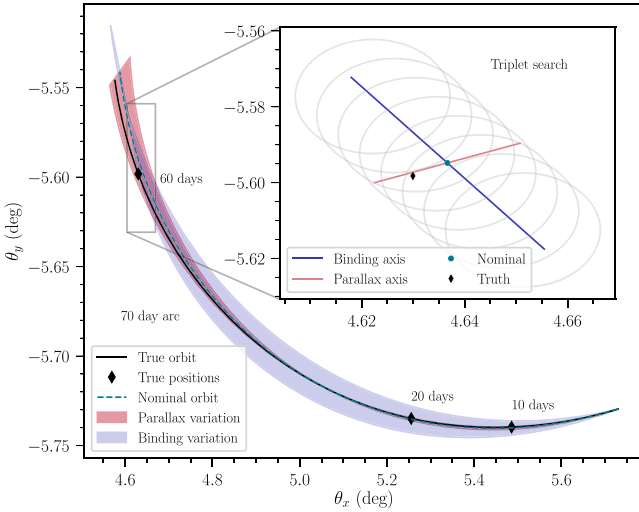
Figure 9. Example of a target orbit at a distance $d = 34$ au, with detections 10, 20, and 60 days past t_0. The search is made with distance bin $\gamma_j = 1/(35\text{ au})$, and $\delta\gamma_j/\gamma_j = 0.05$. The bands show the bounds of predictions vs. time of a third position given the pair at 10 and 20 days, with the orbit fit to this pair with $\dot{\gamma} = 0$. The nominal $\gamma = \gamma_j$, $\dot{\gamma} = 0$ orbit is the dashed line, while the gray and red ranges show the effects of variations in γ ("parallactic") and in $\dot{\gamma}$ ("binding"), respectively. The inset shows the position uncertainties at $t = t_0 + 60$ days. The gray circles show the search region for the third transient, and the diamond is the actual position for this orbit at time t.

area of DECam. (This equation ignores the case where the search circle only partially overlaps exposure ν.) The total number of pairs expected in the search is $N_2 = \sum_{\mu} N_{2,\mu}$. The Y4 search yields $\approx 10^{12}$ pairs (Table 1).

3.2. Finding Triplets

With a pair of detections we can compute $\dot{\alpha}$ and $\dot{\beta}$ as a function of γ and $\dot{\gamma}$. A pair's *nominal* expected position at future exposure at time t is determined by Equations 5(a) and 5(b) with α, β, $\dot{\alpha}$, and $\dot{\beta}$ computed for the bin center γ_j and $\dot{\gamma} = 0$. We further assume that the future position is approximately linear in $(\gamma - \gamma_j)$ ("parallax" axis) and $\dot{\gamma}$ ("binding" axis) as long as we remain within the distance bin range $\gamma_j \pm \delta\gamma_j$ and at $\dot{\gamma}$ small enough to maintain a bound orbit.

To compute the line of variation in (θ_x, θ_y) due to γ deviations (parallax), we calculate the positions for orbits corresponding to α, β, $\dot{\alpha}$ and $\dot{\beta}$ computed for $\gamma = \gamma_j \pm \delta\gamma_j$ and $\dot{\gamma} = 0$.

To compute the line of variation in (θ_x, θ_y) due to non-zero $\dot{\gamma}$ (binding), we first make the assumption that the target orbit is bound, in which case we can write the system's energy more carefully, and derive (as per BK)

$$\dot{\gamma}^2 \leqslant \dot{\gamma}^2_{\text{bind}} \equiv 2GM_{\odot}\gamma^3$$
$$\times (1 + \gamma^2 - 2\gamma \cos\beta_0)^{-1/2} - \dot{\alpha}^2 - \dot{\beta}^2,$$
$$\text{(12)}$$

where β_0 is the target's solar elongation. The line of variations is then derived from positions for orbits corresponding to α, β, $\dot{\alpha}$ and $\dot{\beta}$ computed for $\gamma = \gamma_j$ and $\dot{\gamma} = \pm\dot{\gamma}_{\text{bind}}$.

Figure 9 illustrates how the search region for triplet candidates at some time t is the parallelogram constructed from the parallax axis of γ line of variations and the binding axis of $\dot{\gamma}$ line of variation.

For each pair, we search for triplets in exposures up to 90 days after the second detection. For each exposure that crosses the region of potential third transients, we use its kD tree to rapidly locate for transients lying in a set of circles that cover the parallelogram of potential orbit extrapolations (plus a small contribution for position measurement errors).

One can show that the leading order behavior in γ of the total number of spurious triplets (from randomly positioned transients) is

$$N_3(\gamma) \simeq nN_2(\gamma)A_3(\gamma) \propto n^3\gamma^{7/2}, \quad (13)$$

where A_3 is the area of the search parallelogram.

The Y4 search generates 6×10^{10} triplets (Table 1).

3.3. Growing n-lets

Once a triplet of detections is identified, we can in principle fit an orbit with all six orbital parameters left free. We follow routines similar to those in BK to fit the orbits and determine expected positions and their linearized uncertainties for the circumstances of any DES exposure. We do not make use of the prior in the BK Equations (20) and (21) that favors nearly circular orbits, because it can cause convergence problems for some of the very distant and nearly parabolic TNO orbits that we wish to search. Instead we institute a Gaussian prior on (inverse) distance to force the orbit into our distance bin. The prior contributes to the fit χ^2 as

$$\chi^2_{\text{prior}} = s_{\gamma} \frac{(\gamma - \gamma_j)^2}{\delta\gamma_j^2}, \quad (14)$$

where the strength of this prior is adjusted by setting s_{γ}, and we choose $s_{\gamma} \approx 1$. We also include a prior for bound orbits, defined as

$$\chi^2_{\text{bind}} = b\frac{\dot{\alpha}^2 + \dot{\beta}^2 + \dot{\gamma}^2}{2GM_{\odot}\gamma^3} = \frac{|\text{KE}|}{|\text{PE}|}. \quad (15)$$

Here b, the binding factor, defines the strength of this prior. Note that this is equal to b for a parabolic orbit. We set $b = 4$ for our fits. The χ^2_{bind} is added to the quantity being minimized in the BK code.

The growing process starts with the orbit fitted to a triplet. The position and error ellipse are calculated at all other exposures that the TNO might cross. The kD tree for each potential exposure is searched for transients that lie within the 4σ error ellipse defined by convolving the error ellipse of the orbit prediction at the time of the search exposure with the measurement uncertainty of each transient position on the exposure. For each such transient found, a new n-let is defined, and is queued for its own orbit fit. The addition of transients is iterated for each n-let until no new transients are found to be consistent with the orbit. We also discard any n-let whose orbit fit is significantly unbound, whose best-fit orbit has unacceptably high χ^2 value, or which duplicates a set of transients that have already been examined.

Each time we are attempting to grow an n-let, we calculate the FPR for the addition of the $(n + 1)$th transient. If the 4σ error ellipse on exposure j has area $A_{j,\text{search}}$, and the density of transients on this exposure is n_j, then the total probability of a spurious linkage is

$$\text{FPR} = \sum_j A_{j,\text{search}}n_j, \quad (16)$$

10

where the sum is over all exposures being considered for the $(n + 1)$th transient. Our calculation of FPR currently accounts for CCD gaps and other details of geometry only approximately, but this will be sufficient. Note that as the orbit becomes better defined from higher n and longer arc, the FPR for further additions will shrink. If an n-let has a short arc and we are searching for transient $n + 1$ in a different season's exposure, then the error ellipse may be large, and we will be flooded with false linkages. We therefore do not search an exposure if the contribution of this exposure to the FPR sum would be $A_{j,\text{search}} n_j > 10$. Since the transient catalog density is $\lesssim 200 \deg^{-2}$, this is roughly a requirement that the orbit be localized to an area of $\lesssim 0.05 \deg^2$ if we are to proceed. We do not implement this FPR cutoff until the n-let has linked detections on $\geqslant 4$ distinct nights, since the $A_{j,\text{search}}$ is unavoidably large with $\leqslant 3$ points on the arc.

The growing process terminates when no additional detections are found to match the orbit fit to an n-let. We associate with this terminal n-let the FPR that was calculated for the final *successful* linkage step. Thus the FPR recorded with the n-let estimates the probability that the last detection linked to the orbit is spurious, i.e., a transient that randomly fell within the orbit's error ellipse. In the future this information will allow us to estimate the number of spurious linkages contaminating our TNO catalog. At present, we only make a very mild cut of discarding individual n-lets with FPR > 1. If a terminal n-let has detections in seven or more unique nights and has FPR $< 10^{-3}$, we call it a *secure* orbit, and we remove all of its detections from consideration for linkage to further orbits.

3.4. Reliability of an Orbit

At the end of the linking process, we have to decide which sets of linked detections reliably correspond to multiple detections of the same real solar system object, versus spurious linkages of mixtures of detections of distinct sources or artifacts. In this Y4 search, we use the following criteria to cull the set of unique terminal n-lets to high-reliability candidates.

1. If the number of unique nights on which these detections were seen is NUNIQUE < 6, the n-let is rejected. Of the 132 linkages with NUNIQUE $= 6$ meeting the other criteria, only 52 were confirmed as real by the method of Section 4. The number of n-lets with NUNIQUE $= 5$ is large and certainly dominated by spurious linkages. We defer until the final DES search an effort to extract a reliable candidate set from these. A total of 1684 distinct linkages satisfy this criterion.

2. The time between first and last detections (ARC) must satisfy ARC > 6 months, i.e., we demand detections in distinct DES observing seasons. More stringently, we define ARCCUT to be the shortest arc that remains after eliminating any single night of detections, and demand also that ARCCUT > 6 months. In effect this means that at least two detections must occur outside the season of the triplet that gestates the n-let. Six linkages have ARC < 6 months, and another 1235 also have ARCCUT < 6 months.

3. The χ^2 per degree of freedom from the (prior-less) orbit fit must satisfy $\chi^2/\nu < 4$, which rejects another 19 linkages.

4. The FPR is less than 1. No surviving linkages fail this criterion.

A total of 424 distinct linkages pass these criteria in the Y4 search (see Table 1). The "sub-threshold confirmation" technique described next will serve to remove spurious linkages from the candidate list defined by the above criteria.

4. Sub-threshold Confirmation

We assume without further investigation that all candidates with NUNIQUE > 10 are real TNOs, since the calculated FPRs for these are extremely small. For objects with $6 \leqslant$ NUNIQUE $\leqslant 10$, we test the reality of each candidate TNO by searching for its presence in exposures that did *not* yield a detection of the source, but which the best-fit orbit suggests should contain an image of the object. The concept here is: if the object is real, it is lurking just below detection threshold in these non-detection images and, by stacking such exposures along the orbit, we will obtain a significant detection. If, however, the orbit is spurious, then there should be no excess flux in the non-detection images along the (meaningless) orbit. Given that we typically have ≈ 10 non-detections (excluding the Y band), the non-detection stack should be ≈ 1.25 mag deeper than a typical single image.

The non-detection images are by definition going to have lower mean S/N ratio on a real TNO than the typical detection image. This could be because of poorer observing conditions, or being in filters with less favorable S/N given the color of the TNO, or at fainter points on the light curve of a given TNO. Furthermore there are no degrees of freedom in this sub-threshold confirmation significance, because the orbit is fixed to the best fit to the detected transients. So the appearance of a signal even at S/N $= 4$ in the non-detection stack should be considered a strong confirmation.

We proceed by first measuring a flux for the putative TNO in every image μ (both detections and non-detections) that contains the best-fit orbit. For exposure μ in band b, we compute a windowed, sky-subtracted flux $f_{\mu,b}$ as

$$f_{\mu,b} = k_\mu \sum_j (s_{\mu,j} - \hat{s}_\mu) W_\mu(\boldsymbol{x}_j). \tag{17}$$

Here, $s_{\mu,j}$ is the photon count at pixel $\boldsymbol{x}_j$, and $\hat{s}_\mu$ is the sky background flux, computed by taking the mean flux in an annulus centered at the nominal position and with inner radius $8''$ and outer radius $10''$. For the photometry window $W_\mu(\boldsymbol{x}_j)$ we adopt a circular Gaussian centered on the position predicted from the orbit, and having a FWHM of $1''$. This window will retrieve near-optimal S/N ratio for the putative TNO in typical DES seeing. The factors k_μ remove the variations in the photometric zero-points of the exposures, placing fluxes on a common scale (Burke et al. 2017). The rms noise $\sigma_{\mu,b}$ in $f_{\mu,b}$ is calculated by propagating the Poisson noise of the $s_{\mu,j}$ through Equation (17).

We need to remove the contribution of static sources from $f_{\mu,b}$. To do so we apply (17) to the coadd image at this location of sky to obtain flux $f_{\mu,b,\text{coadd}}$ and noise $\sigma_{\mu,b,\text{coadd}}$. If the static flux is a significant fraction of the inferred flux, we discard this exposure from the calculation. The criteria for rejection are $f_{\mu,b} < 3 f_{\mu,b,\text{coadd}}$ (the TNO flux does not dominate the static flux) and $f_{\mu,b,\text{coadd}} > 5\sigma_{\mu,b,\text{coadd}}$ (nonzero static flux is

confidently detected). Single exposures failing this cut are ignored in further evaluation of their TNO orbit.

The inverse variance weighted total flux, then, coming from the remaining images is

$$\hat{f}_b = \frac{\sum_\mu f_{\mu,b}\, \sigma_{\mu,b}^{-2}}{\sum_\mu \sigma_{\mu,b}^{-2}}, \quad (18)$$

with variance

$$\mathrm{Var}(\hat{f}_b) = \frac{1}{\sum_\mu \sigma_{\mu,b}^{-2}}. \quad (19)$$

The *significance* of a detection in band b, then, is

$$\mathcal{S}_b = \frac{\hat{f}_b}{\sqrt{\mathrm{Var}(\hat{f}_b)}}. \quad (20)$$

For visual inspection, we also combine the individual exposures' images of the putative TNO using inverse-variance weighting:

$$\mathrm{Img}_b = \frac{\sum_\mu k_\mu \mathrm{Img}_{\mu,b}\, \sigma_{\mu,b}^{-2}}{\sum_\mu \sigma_{\mu,b}^{-2}}, \quad (21)$$

where $\mathrm{Img}_{\mu,b}$ is a 50×50 pixel image cutout centered on the detection at exposure μ.

To compute the *total significance*, we combine all detections in the *griz* bands by first transforming all *giz* fluxes into an *r*-band flux, assuming nominal colors corresponding to the bimodality break for Centaurs: $g - r = 0.75$, $r - i = 0.25$ and $r - z = 0.5$ (Ofek 2012; Pike et al. 2017). To confirm an orbit, we only use the images in which there is no detection in the Final Cut catalog. We define the "sub-threshold significance" (STS) to be the value of $\mathcal{S}_b$ from Equation (20) evaluated only on these non-detection images. Spuriously linked detections cannot contribute to this total significance. Non-detection images taken within 1 hr of a detection are omitted from this summation, so that a spuriously linked asteroid (or image defect) cannot recur in a non-detection image and contaminate the STS. In other words, we want the STS to be statistically independent of the detections in the absence of a true TNO.

Figure 10 shows an example of a real TNO that passes this test. Figure 11 shows a spurious linkage.

In addition to the value of STS, we also vet all 424 candidates passing the basic parametric cuts of Section 3.4 by visually inspecting postage stamps of all images of the putative orbit. We also view the summed *griz* images (following Equation (21) and using the nominal colors) created both using all the images, and the image created from just the non-detection images. Each candidate received a score of R (real), F (false) or M (maybe, corresponding to an unsure classification) independently by three of the authors (P.B., G.B., and M.S.). In every case, at least two graders agree, and we accept the majority classification. The visual inspection also identifies non-detection images in which the STS calculation is being contaminated by any static sky object or unmasked defect that sneaked past the cuts on coadd flux described above. For these cases we recalculate the STS after purging this defective exposure. Note that the grading was done while blind to the orbital elements of the detection.

Figure 12 shows that the 424 orbit candidates fall into two distinct groups on the plane of STS versus N_{images}, the number of non-detection images contributing to STS. These groups are cleanly separated by the parabola STS $= 2\sqrt{N_{\mathrm{images}}}$, and every candidate graded as R (F) falls to higher (lower) STS than this curve, suggesting that cutting objects to the left of this curve is a very efficient means of removing spurious linkages. Our confidence in this cut is boosted by noting that the linkages failing this cut are generally much worse fits to an orbit than the retained sample. As illustrated by Figure 15, however, the χ^2/ν statistic is not by itself a sure-fire discriminant between real and spurious linkages. We might indeed expect that some spurious linkages attain low χ^2 by luck, and also that some true TNOs might have inflated χ^2 values because they are binaries with significant photocenter motion about the center of mass. So we do not impose any stricter cut on χ^2/ν.

A total of 316 linkages pass the STS cut, and comprise the complete sample of detections from the Y4A1 DES wide-survey search; see Table 1.

The weighting of the different bands in the STS value yields optimum (high) values for objects with mean TNO colors. For individual objects with colors deviating from this mean, the STS we compute is non-optimal (lowered). So the technique, applied with fixed nominal weighting, cannot produce false positives, but might produce a false negative if an object's colors are significantly different from those chosen. The calculation is, however, robust: object 2013 SN$_{102}$ is one of our reddest at $g - r \approx 1.23$ (compared to the nominal $g - r = 0.75$; the $r - i$ and $r - z$ colors of the object are within 20 mmag of the nominal colors). Its STS is ≈ 22.7 with nominal weighting and rises to ≈ 24.1 by computing this value with weights optimized to its colors. Thus the nominal weighting yields STS only 6% lower than optimal in this extreme case.

The STS test can be also be applied to objects that are too faint to be recovered in the survey, but whose orbits are known to good precision. As an example, we have measured the STS of 2016 QU$_{89}$, discovered on the deep DES fields (Khain et al. 2018) and too faint to be detected in the wide survey. This object was recovered in only two of the images we analyzed here, despite being inside a functional CCD in 17 images. We have measured its STS to be 24.6, being well above the required $2\sqrt{N_{\mathrm{images}}} \sim 8.2$ required to recover it.

Finally, we note that the tools presented here allow us to distinguish real from spurious five-night detections by repeating the STS test, although this will require us to evaluate many spurious linkages. The entire linkage process can also be extended to distances closer than 30 au, but at a significant increase in computational expense (see Equations (11) and (13)), perhaps requiring a trade-off between the searched distances (i.e., γ) and the maximum time span of the pairs and triplets (Δt).

5. Completeness Testing with Synthetic TNOs

In order to test our linking efficiency, we insert a synthetic population of TNOs ("fakes") into our transient catalog that simulate the observational properties a real object would have. This is not an end-to-end simulation: the fakes are inserted into the catalogs, not the images. The cost of doing the latter and reprocessing all the images would be prohibitive. This shortcut is, however, acceptable, since the point-source detection efficiencies described in Section 2.6 allow us to assess the
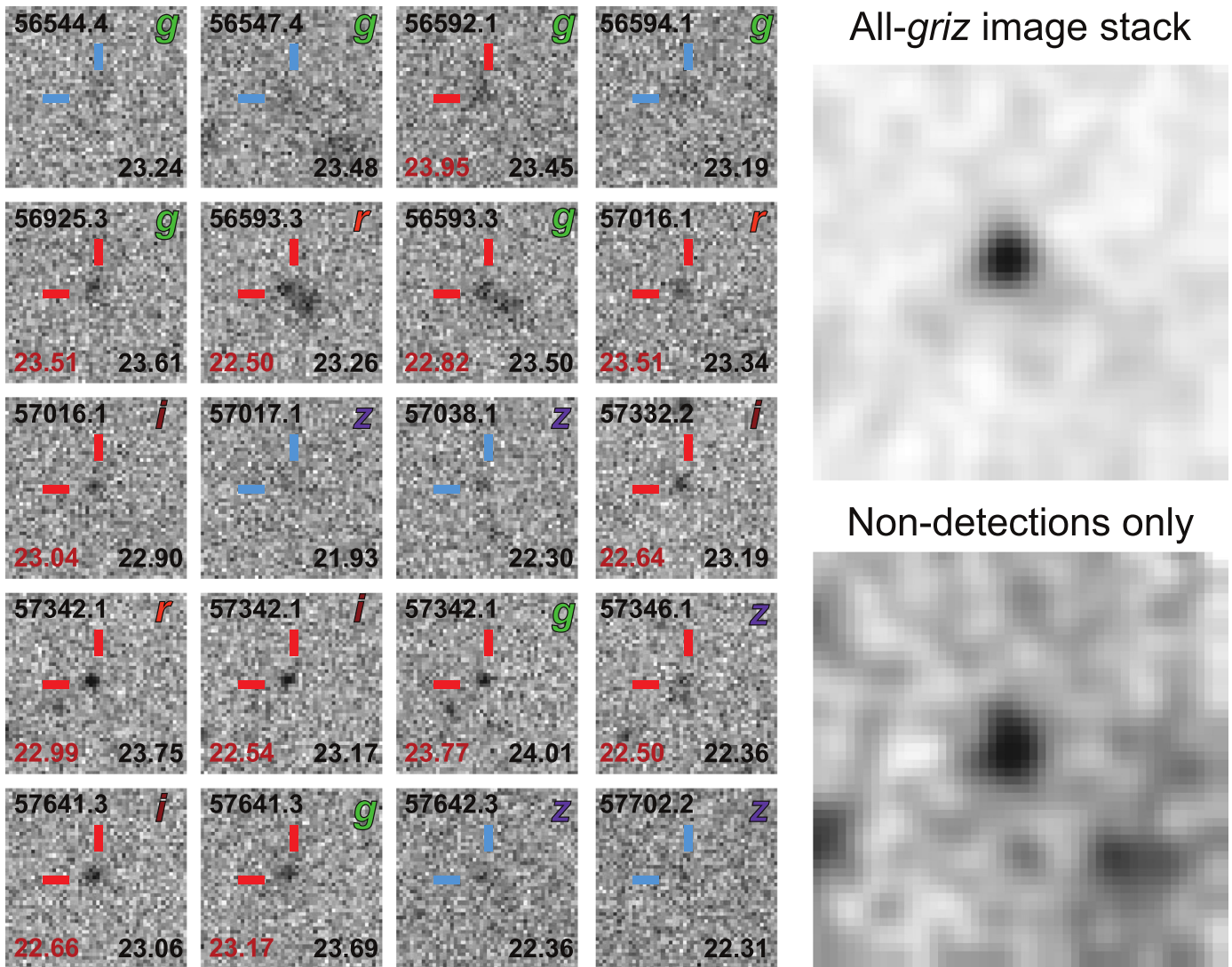
Figure 10. Left: postage stamps of the detected and expected positions for one of the recovered TNOs with NUNIQUE = 8. The top of each stamp shows the modified Julian date when the exposure was taken and its band, with m_{50} for the exposure at lower right. Exposures where the object was detected are marked in red crosshairs and have the measured magnitude listed on the lower left. Exposures of the putative TNO which did not yield a detection are marked with blue crosshairs. Right: summed *griz* images (all images: top; non-detections only: bottom) convolved by a 1″ Gaussian kernel. The lower-right image shows a highly significant detection (STS = 12.93), and is considered confirmed.

detectability of a TNO of given magnitude in a given exposure. This method does not, however, account for the inefficiency in transient detection that arises when TNOs fall on or near stationary sources (such that they are part of blended detections, or flagged as static sources), or when TNOs lie on CCD defects or other artifacts (such that they are flagged as defective and ignored). A few percent of the active imaging area is lost to such effects in typical exposures. Image-injection experiments under way on the completed DES imagery will quantify this loss and be incorporated into the detection simulator that will accompany the final DES TNO catalog (Suchyta et al. 2016).

5.1. Simulating the DES Observations

The process for simulating the transient-catalog entries for a TNO of given orbital parameters and magnitude m is as follows.

i. We find all exposures for which the DECam FOV contains the TNO position given its orbit.

ii. An observed position for the TNO is derived by adding observational error to the position predicted by the orbit. Currently the observational error is drawn from the distribution of errors for all point sources in the image (including both shot noise and the atmospheric turbulence contribution per Equation (2)); in the future we will properly track the errors versus source magnitude.

iii. We check whether the "observed" position lies within a functional DECam CCD, i.e., we would have collected an image of this TNO. If this is true, this is considered an *observation*.

iv. We compute the value of $p(m)$ from Equation (4) with the fitted parameters for this exposure and compare to a random value r between 0 and 1. If $p(m) > r$, this observation is considered a *detection* and is entered into the transient catalog.
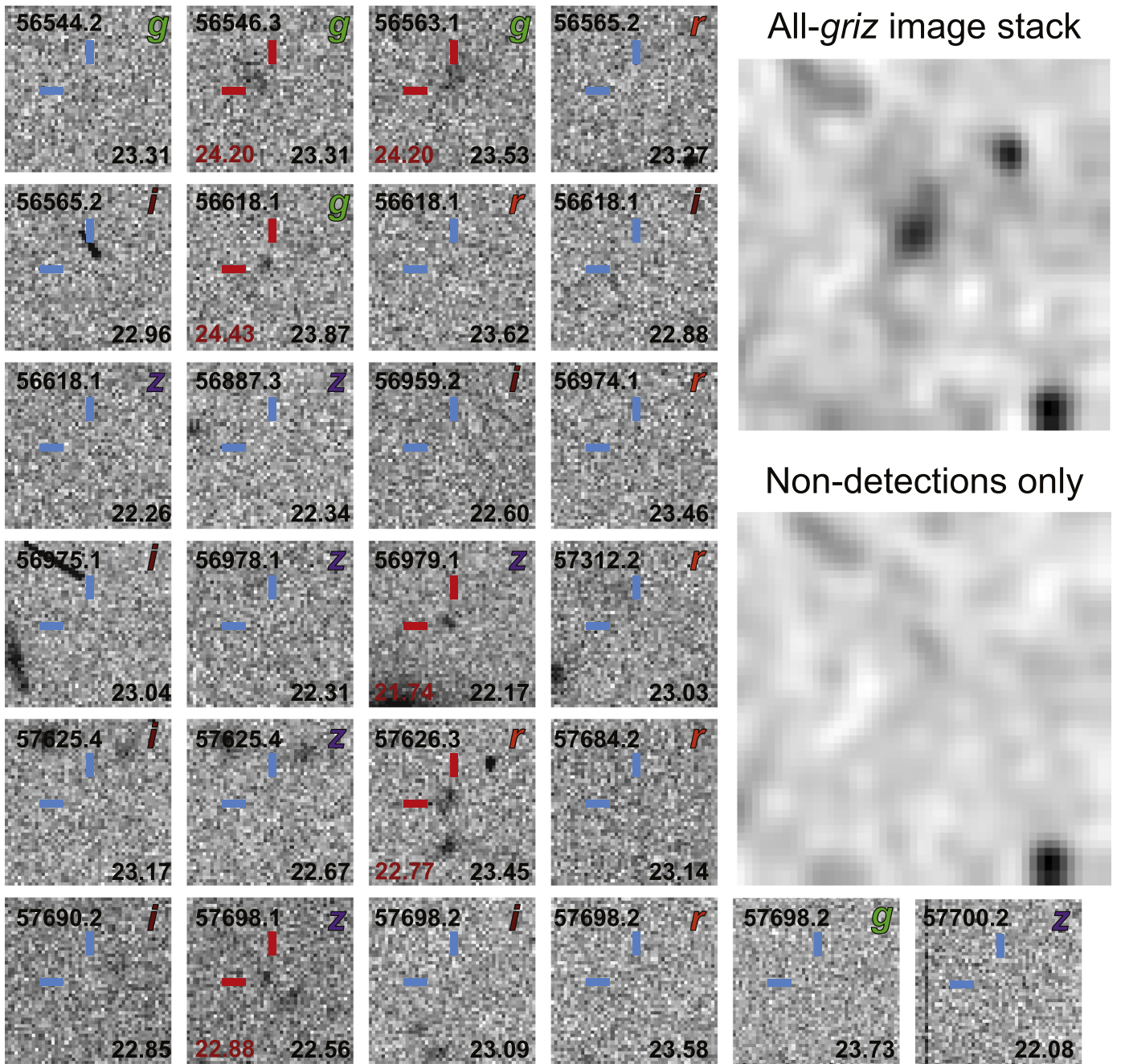
Figure 11. Similar to Figure 10, but showing a candidate that does not pass the sub-threshold significance test. The STS of this candidate is −0.16.

v. For completeness, a random magnitude error is drawn from the magnitude error distribution determined for this exposure and added to the truth magnitude, for each synthetic transient. Our linking algorithm makes no use of the detected magnitude, so this is irrelevant.

This process does not simulate the loss of TNOs due to potential overlap with other sources or image artifacts, which as noted above creates a loss of a few percent of sources. Note also that no light-curve variation is placed on the simulated sources.

5.2. Fake Population Inserted into the Transient Catalog

We generate a population of synthetic TNOs that is intended to sample the full phase space of possibly detectable orbits and magnitudes, with no intention of mimicking the true TNO population. We generate the fakes by sampling the barycentric phase space $\{x_0, y_0, z_0, \dot{x}_0, \dot{y}_0, \dot{z}_0\}$ at a reference time t_0 near the survey midpoint. To generate the position vector, we sample the unit sphere by constructing uniformly distributed angles with a Fibonacci lattice (see, e.g., González 2010) in equatorial coordinates, and discard all points well outside the DES footprint. Each fake is assigned a random barycentric distance from a distribution placing half of the fakes uniformly in the range 30–60 au and half logarithmically distributed between 60 and 2500 au. Similarly, the velocities are sampled by placing angles on a spherical Fibonacci lattice, and assigning a velocity $v = f^{1/3} v_{\mathrm{esc}}(d)$, where $v_{\mathrm{esc}}(d)$ is the escape velocity at the barycentric distance, and f is a uniform deviate between 0 and 1.

14
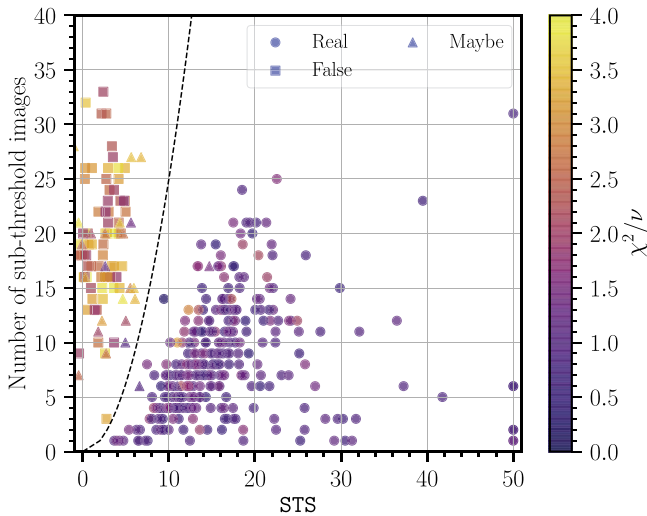
Figure 12. STS vs. number of images used in the sub-threshold sum, as well as a color code for χ^2/ν. The symbol shapes encode the R, F, M status derived from visual inspection. The dashed curve is the STS $= 2\sqrt{N_{\text{images}}}$ parabola, which cleanly divides all "Real" from "False" linkages and separates the two obvious groupings in the plot. We consider all 316 linkages lying to the right of the parabola as being confirmed TNOs.

Each fake is also assigned an *r*-band magnitude, independent of its distance, sampled from a uniform distribution between $m_{\text{bright}} = 20$ and $m_{\text{faint}} = 24.5$, spanning the range in which we expect our Y4 discovery efficiency to go from near unity to zero. Each TNO's magnitude is assumed to be constant (i.e., there is no light curve for the object). The colors are fixed and chosen to be similar (but not identical) to those of (136199) Eris (Brown et al. 2005) as observed by DES: $g - r = 0.55$, $r - i = 0.07$, $r - z = -0.02$, and $r - Y = -0.04$.

The transient catalog used in the search includes these fakes, and the process is blinded in that the linking algorithms make no distinction between real and fake transients.

5.3. Completeness Estimates

Figure 13 shows (at left) the frequency of observations and detections for a population of ≈200,000 fakes. Here we can see that the typical TNO is observed on ≈20 distinct nights of the Y4 data, with a tail to low values for TNOs that move in or out of the survey footprint during the survey. This will occur near the edges and along the thin equatorial stripe of the footprint. Fainter objects are detected in fewer observations, once $m_r > 21$. In the range $23 < m_r < 23.5$, about half of fake TNOs are "recoverable" by our criterion that they have NUNIQUE $\geqslant 6$. The right-hand panel integrates over all orbital parameters to give the effective survey area as a function of m_r, indicating that the detection and linkage are highly complete for $m_r < 23$, and 50% complete at $m_r \approx 23.3$ (assuming that all colors are Eris-like). Figures 14 shows the recovery efficiency as a function of inclination and bary-centric distance, indicating that there is very little dependence on the orbital properties of an object at fixed apparent magnitude. The DES footprint is much broader than a typical TNO's orbital path, except for the narrow equatorial stripe, meaning that the detectability of a TNO is almost entirely a function of apparent magnitude once it has distance >30 au. A minor exception is for TNOs with inclination near 0° or 180°,

for which a significant fraction of our coverage is in the narrow strip.

5.4. Completeness over Previously Known TNOs

A search of the MPC database for known TNOs that were within the FOV of at least six of the DES Y4 *griz* exposures shows that all such objects above our estimated $r = 23.3$ mag 50% completeness level are indeed among our 316 detections. The brightest of these known TNOs that we do *not* rediscover is 2013 RY$_{108}$, at $r = 23.47$, which was in fact discovered from the deep supernova-search images in DES. It is in the FOV for 13 wide-survey exposures on nine distinct nights, but was only detected in three of these exposures. This is fully consistent with our estimated completeness thresholds. The final DES TNO search will have a lower SE detection threshold, and more exposures, that should enable discovery of many similar TNOs.

6. Catalog of DES TNOs

In Table 2, we present the 316 objects that pass the STS test shown in Figure 12. Additionally, distinct objects found in other searches of DES data and reported to the MPC are listed in Table 3 (Khain et al. 2020). The other searches include data from the deeper, high-cadence supernova fields, and also discovered objects at distances <30 au, which would be missed by the Y4 search. Since the other searches are not as homogeneous across the DES footprint as the Y4 search, the statistical summaries presented here include only objects detected in the Y4 search.

The histogram of the astrometric χ^2 per degree of freedom of best-fit orbits is presented in Figure 15. This histogram suggests that our positional accuracies are estimated to good precision, since the peak is close to $\chi^2/\nu = 1$. More precisely, the mean $\langle\chi^2/\nu\rangle = 1.13$ suggests that our errors are slightly underestimated. A similar conclusion can be drawn from comparing to the χ^2/ν distribution of the implanted fake detections, for which we know the observational errors exactly, and which yield a slightly lower distribution. An 11% increase in the astrometric covariance matrices, corresponding to a 5% increase in errors on positions and orbital elements in real detections, leads to good agreement between the fitted χ^2 and a true χ^2 distribution. This potential 5% underestimate of orbital errors should be considered a maximum value, since some of the inflated χ^2 values could instead arise from small photocenter motions in binary TNOs. A significant fraction of cold classical TNOs ($i \lesssim 5°$) are expected to be binaries (Stephens & Noll 2006), and we would not want to cut these from our sample. The only one of our detected TNOs in W. Grundy's list of known binaries[35] is Eris, a large-mass-ratio binary for which photocenter motion should be small, so we cannot yet verify any cases of binary-inflated χ^2. We note that $\langle\chi^2/\nu\rangle$ for the cold classicals is higher than average at 1.31, but we have not yet investigated whether this is attributable to binaries.

Figure 16 compares the quality of the orbits obtained here to those from OSSOS (Bannister et al. 2018), where we see that the mean error of the DES detections' semimajor axis is lower than those of OSSOS, without the need for targeted followup. The median DES error on *a* of a classical Kuiper Belt object is
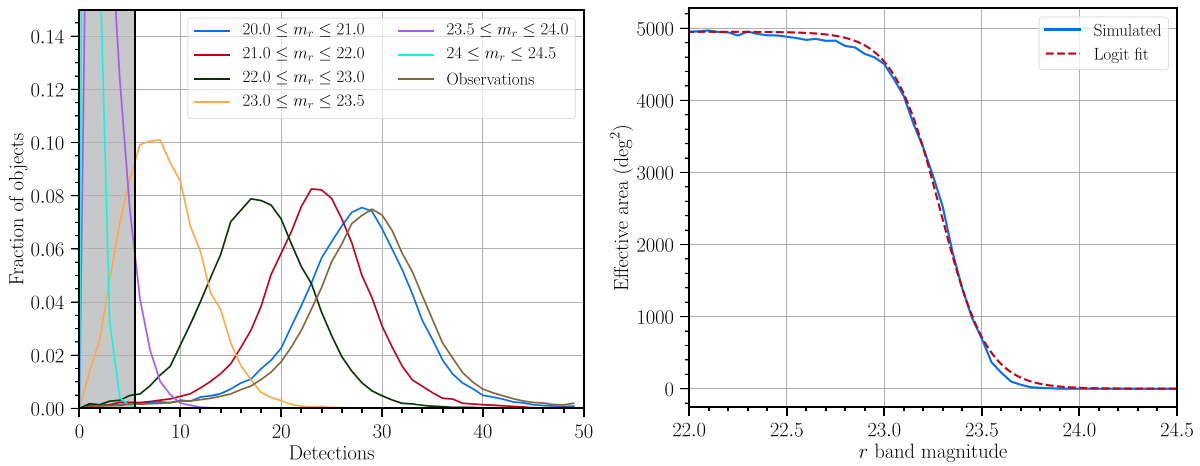

Figure 13. Left: the brown curve plots the distribution of the number of DES observations (i.e., the TNO falls on a CCD) for a sample of 196,663 simulated TNOs evenly distributed in the DES footprint. The other curves at left show the distribution of number of these observations that would result in detections (i.e., signal above detection threshold), as a function of r band magnitude The shaded area indicates the region with less than six detections—there are many spurious linkages with less than six detections, so we do not yet report TNO detections in this regime. Right: effective search area for an object vs. magnitude, averaged over orbital parameters for the simulated TNO population. An object is considered as recoverable if it is detected in more than six unique nights. A logit fit (similar to Equation (4)) to this function shows that $m_{50} = 23.29$.
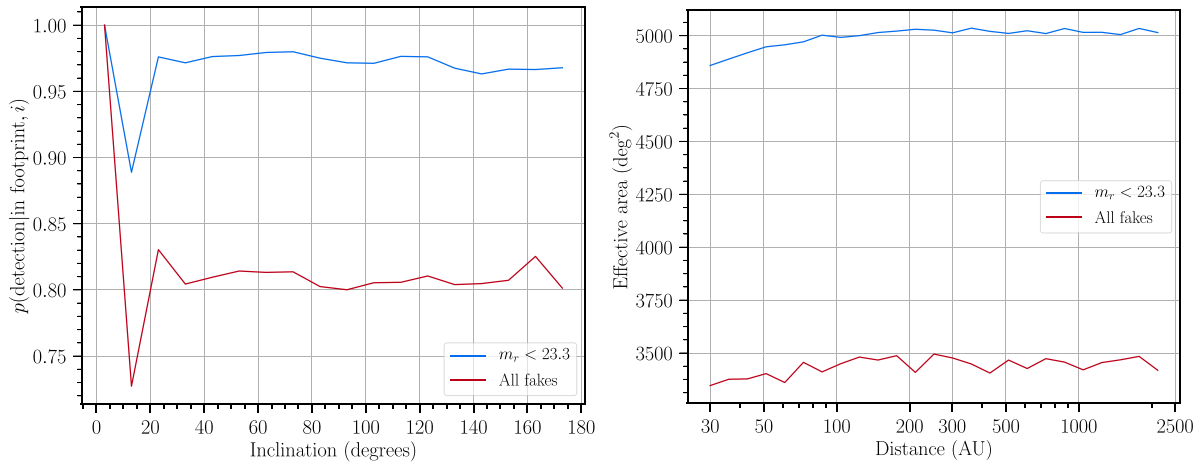
Figure 14. Left: probability of recovery of an object with a given inclination on the complete regime (blue, $m_r < 23.4$) and for all simulated objects (red). Since the survey's longitudinal coverage at low ecliptic latitudes is not as extensive as at high latitudes (see Figure 1), objects with $i \lesssim 10$ and $i \gtrsim 170°$ have a higher chance of leaving the nominal footprint. Right: effective search area as a function of barycentric distance, showing very little dependence of recovery probability on an object's distance.

≈ 1.5 lower than in OSSOS, and will decrease with inclusion of the final 2 yr survey data.

The semimajor axes, eccentricities and inclinations for all Y4 objects are plotted in Figure 17, their magnitudes in Figure 18, and their locations for a fixed epoch in Figure 19. We highlight the following properties of our sample.

1. Of the 316 objects reported here, 139 are reported here for the first time, and 245 are DES discoveries. In Table 4, we further divide the objects by dynamical classes following Gladman et al. (2008). The full methodology is presented in Khain et al. (2020). The classification is made by integrating 10 clones of each object for 10 Myr, and resonances of the form p: q, p, $q \in [1, 26]$ are identified using an automated system.

2. We have 54 detached objects in our sample, one of the largest samples of this population to date, although some of the detached objects near high-order resonances with

Neptune might end up reclassified as resonant as the orbits are refined.

3. There are 87 confirmed resonant objects, with another 13 resonant candidates. Of the confirmed objects, seven are Neptune Trojans (four of them new to this work), 30 Plutinos and two in the 4:1 resonance. There is one 16:3 resonant candidate ($a \sim 91.1$ au).

4. There are seven extreme TNOs ($a > 150$ au, $q > 30$ au), including one $a > 250$ au object new to this work.

5. Since most of our area is far from the ecliptic, almost half of our sample consists of objects with $i > 20°$.

6. The flattened distribution of the Kuiper Belt is readily apparent, and indeed we have discovered no TNOs more than $55°$ from the ecliptic plane despite substantial sensitivity outside this range (compare Figure 19 to 14).

7. The truncation of the classical Kuiper Belt (Allen et al. 2001) at the 2:1 resonance is also apparent, demonstrated

16

Table 2
DES Trans-Neptunian Objects

Column Name	Unit	Description
MPC		Minor Planet Center object designation
DES		DES object designation
a (a)	au	Semimajor axis of the best-fit orbit
σ_a (sigma_a)	au	Uncertainty in a
e (e)		Eccentricity
σ_e (sigma_e)		Uncertainty in e
i (i)	deg	Inclination
σ_i (sigma_i)	deg	Uncertainty in i
ω (aop)	deg	Argument of perihelion
σ_ω (sigma_aop)	deg	Uncertainty in ω
Ω (lan)	deg	Longitude of ascending node
σ_Ω (sigma_lan)	deg	Uncertainty in Ω
T_p (T_p)	UTC Julian date	Time of perihelion passage
σ_T (sigma_T)	days	Uncertainty in T_p
q (q)	au	Perihelion distance
σ_q (sigma_q)	au	Uncertainty in q
d (d)	au	Discovery distance (geocentric)
σ_d (sigma_d)	au	Uncertainty in d
m_r (m_r)	mag	Mean r band magnitude
σ_m (sigma_m)	mag	Uncertainty in m_r
H_r (H_r)	mag	Absolute magnitude in band r
σ_H (sigma_H)	mag	Uncertainty in H_r
NUNIQUE		Number of unique nights of detections
NDETECT		Number of detections
χ^2 (CHI2)		χ^2 of the orbit fit ($\nu = 2 \times$ NDETECT $- 6$)
x, y, z (x, y, z; 3 columns)	au	ICRS-oriented positions
v_x, v_y, v_z (vx, vy, vz; 3 columns)	au/year	ICRS-oriented velocities
$\Sigma_{\mu,\nu}$ (Sigma_mu; 21 columns)	(au, au/yr)^2	μ, ν element of the state vector covariance matrix
Class		Dynamical classification

Note. The description of each column is given here. The table is provided in a machine-readable format. Each uncertainty is the 1σ uncertainty marginalized over all other orbital parameters. All of the elements reported are barycentric and refer to epoch 2016.0.
(This table is available in its entirety in FITS format.)

by the small absence of low-eccentricity objects past 48 au (upper panel of Figure 17).

8. The sample contains several extreme TNOs and several high-inclination ($i > 40°$) objects that are difficult to produce in basic formation scenarios, and should be highly constraining for alternative dynamical scenarios.

Detailed characterization of the TNO populations will be presented in future publications.

7. Summary and Prospects

We report 316 TNOs found in the first four years of data from the 5000 deg^2 DES. The astrometry for this sample was calibrated to *Gaia* Data Release 1. This search is complete to magnitude $m_r \approx 23.3$. DES is a temporally sparse survey, requiring us to develop new methods to identify moving objects and link them into orbits. A technique applied here to
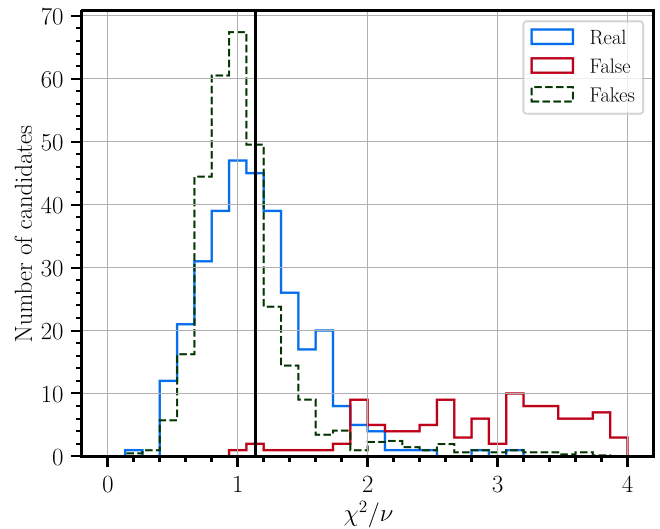
Figure 15. χ^2 per degree of freedom ν for all 424 candidate orbits, with the blue curve representing the 316 confirmed linkages, and the red representing the candidate orbits rejected as spurious linkages. The black line marks the mean of the blue histogram, $\langle \chi^2/\nu \rangle = 1.13$. The dashed curve represents the χ^2/ν distribution for the 1727 fakes inserted into the catalog and retrieved by the linking process. The "Fakes" histogram is normalized to the same sum (316) as the real detections for easy comparison, showing the real sources to be only slightly poorer fits to their orbits, on average.

Table 3
Known Trans-Neptunian Objects Found in Other Searches of DES Data

Column Name	Unit	Description
MPC		Minor Planet Center object designation
a (a)	au	Semimajor axis of the best-fit orbit
σ_a (sigma_a)	au	Uncertainty in a
e (e)		Eccentricity
σ_e (sigma_e)		Uncertainty in e
i (i)	deg	Inclination
σ_i (sigma_i)	deg	Uncertainty in i
ω (aop)	deg	Argument of perihelion
σ_ω (sigma_aop)	deg	Uncertainty in ω
Ω (lan)	deg	Longitude of ascending node
σ_Ω (sigma_lan)	deg	Uncertainty in Ω
T_p (T_p)	UTC Julian date	Time of perihelion passage
σ_T (sigma_T)	days	Uncertainty in T_p
Reason		Reason the object was missed[a]

Notes. The details of this search are explained elsewhere (Khain et al. 2020).
[a] d: deep fields, m: missing from transient catalog, l: failed linkage, c: geocentric distance closer than 30 au, s: short arc (i.e., ARCCUT < 6 months).
(This table is available in its entirety in FITS format.)

TNOs for the first time (to our knowledge) is to confirm orbital discoveries using the "sub-threshold significance" statistic, whereby we stack along the orbit using only exposures that are statistically independent of those used to discover the object. This provides a very clear distinction between real sources and spurious linkages. The need for this arises from the fact that, in a survey as large as DES, distinct asteroid detections or defects can align so as to mimic a true TNO on as many as seven distinct nights spread over multiple years.

The large contiguous field and homogeneous coverage of DES is shown to yield a selection function that is nearly independent of orbital elements, as long as the orbit and source
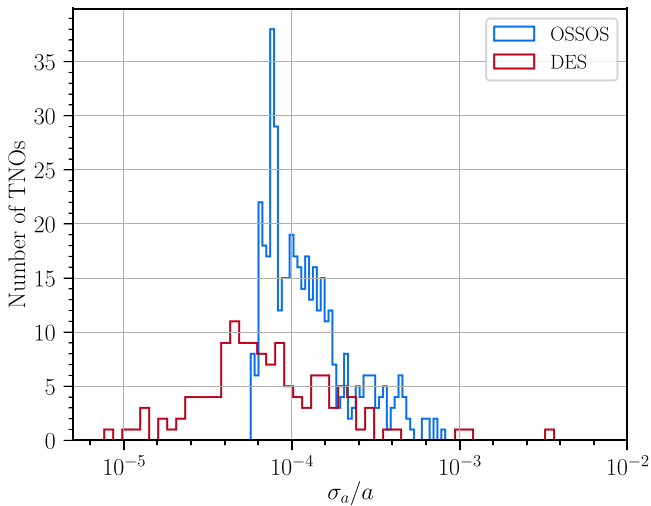
Figure 16. Comparison of σ_a/a for the 436 OSSOS (Bannister et al. 2018) classical TNOs to the 134 from DES. The median DES orbital uncertainty is $\approx 1.5\times$ lower than than those from OSSOS, without the need for targeted followup observations.

magnitude yield detections on at least six DES exposures spanning multiple seasons. This will make it relatively straightforward to compare the DES Y4 catalog to candidate models of TNO populations. Each detected object has already been observed in five filters with multiple years' arcs, and the survey spans a large range of ecliptic latitude, making it valuable for comparisons to theory. We plan, however, to defer the most detailed comparisons until we apply our methods to the full DES data set.

We expect many improvements for the final analysis of DES data from the full six years of the survey. The SExtractor (Bertin & Arnouts 1996) detection filter has been changed to better approximate the PSF for DES images, and the detection threshold has been lowered. These should yield 0.3 mag fainter m_{50} with only modest increase in the size of transient catalog. We also will have full 10-tiling coadds, leading to more efficient rejection of stationary objects. With the six years of data, we expect that most orbit arcs will all be at least three years long, and our photometry will be improved from multiple epochs of data. In addition, our astrometry will be calibrated to *Gaia* Data Release 2 (Gaia Collaboration et al. 2018).
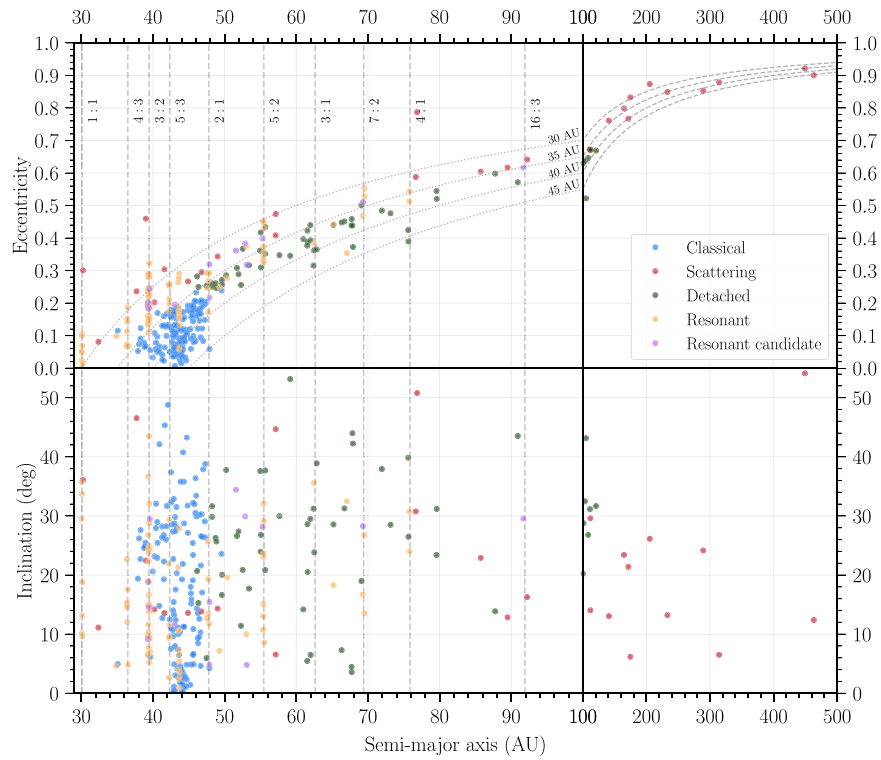
Figure 17. Semimajor axis vs. eccentricity and inclination for the 316 TNOs found in DES data. The approximate semimajor axis location of some resonances with Neptune is shown by the dashed vertical lines, and the dotted lines in the upper panel represent lines of constant perihelion, color-coded by which dynamical population each object belongs to. Table 4 lists the number of objects per dynamical class and resonance. We note here that some objects near high-order mean motion resonances with Neptune might be identified as "detached" due to uncertainties in the orbit parameters.
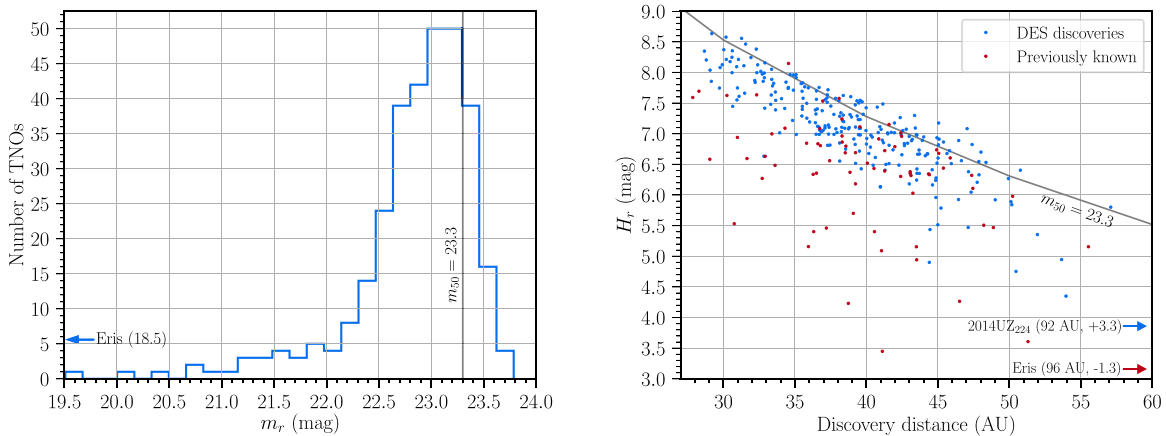
Figure 18. Left: histogram of apparent r-band magnitudes for all recovered objects, with the black line indicating the magnitude of 50% completeness of the survey at $m_{50} = 23.3$. Right: discovery distance vs. absolute r magnitude for all objects, color-coded to indicate whether the object was known before DES or not. Note that, in both figures, Eris is indicated to be outside the plot's range. 2014 UZ_{224} is outside the range of the second figure as well. The magnitudes (m_r and H_r) and distances for these objects are indicated in parenthesis.
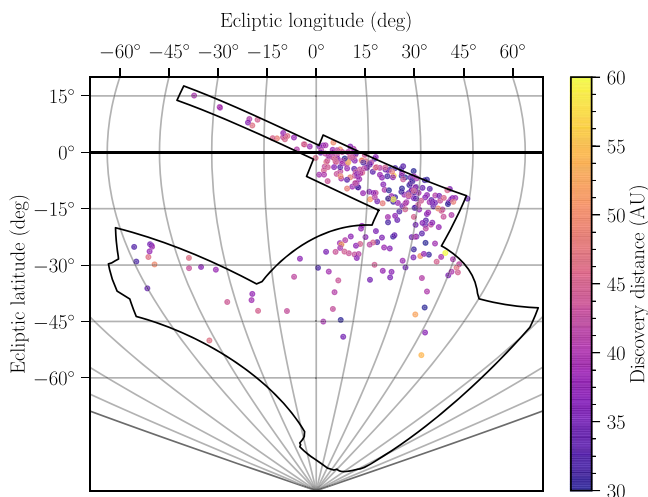
Figure 19. Location of the TNOs reported here at the epoch JD = 2457388.4 (2016 January 1). The color scale represents the discovery distance (note that two of the objects were found at $d > 90$ au). The black line bounds the survey footprint. Note the paucity of TNO detections at ecliptic latitudes below $-50°$.

Table 4
Dynamical Classification of the 316 Objects Following Gladman et al. (2008)
(See Khain et al. 2020 for Details)

Dynamical Class	Number of Objects
Classical belt	134
Scattering	28
Detached	54

Mean-motion Resonators with Neptune	Number of Objects
1:1 (30.1 au)	7
5:4 (34.9 au)	1
4:3 (36.3 au)	7
3:2 (39.4 au)	30 + 4 candidates
5:3 (42.3 au)	6
12:7 (43.1 au)	1 candidate
7:4 (43.7 au)	12
2:1 (47.7 au)	5 + 2 candidates
21:10 (49.3 au)	1
13:6 (50.4 au)	1
9:4 (51.7 au)	1 candidate
7:3 (52.9 au)	1 + 2 candidates
5:2 (55.4 au)	8 + 1 candidate
3:1 (62.6 au)	1
16:5 (65.4 au)	1
10:3 (67.1 au)	1
7:2 (69.4 au)	3 + 1 candidate
4:1 (75.8 au)	2
16:3 (91.9 au)	1 candidate
Total	316

Note. The resonant objects are presented in order of increasing semimajor axis, with the approximate value presented in parenthesis.

ORCID iDs

Pedro H. Bernardinelli ● https://orcid.org/0000-0003-0743-9422
Gary M. Bernstein ● https://orcid.org/0000-0002-8613-8259
Masao Sako ● https://orcid.org/0000-0003-2764-7093
Tongtian Liu ● https://orcid.org/0000-0001-5677-5188
William R. Saunders ● https://orcid.org/0000-0002-8737-742X
Tali Khain ● https://orcid.org/0000-0001-7721-6457
Hsing Wen Lin ● https://orcid.org/0000-0001-7737-6784
David W. Gerdes ● https://orcid.org/0000-0001-6942-2736
Dillon Brout ● https://orcid.org/0000-0001-5201-8374
Fred C. Adams ● https://orcid.org/0000-0002-8167-1767
Juliette C. Becker ● https://orcid.org/0000-0002-7733-4522
Larissa Markwardt ● https://orcid.org/0000-0002-2486-1118
James Annis ● https://orcid.org/0000-0002-0609-3987
D. Gruen ● https://orcid.org/0000-0003-3270-7644
R. A. Gruendl ● https://orcid.org/0000-0002-4588-6517
D. L. Hollowood ● https://orcid.org/0000-0002-9369-4157
R. Miquel ● https://orcid.org/0000-0002-6610-4836
E. S. Rykoff ● https://orcid.org/0000-0001-9376-3135
G. Tarle ● https://orcid.org/0000-0003-1704-0781
A. R. Walker ● https://orcid.org/0000-0002-7123-8943

References

Abbott, T. M. C., Abdalla, F. B., Allam, S., et al. 2018, ApJS, 239, 18
Acton, C., Bachman, N., Semenov, B., & Wright, E. 2018, P&SS, 150, 9
Acton, C. H. 1996, P&SS, 44, 65
Adams, F. C. 2010, ARA&A, 48, 47
Alexandersen, M., Gladman, B., Kavelaars, J. J., et al. 2016, AJ, 152, 111
Allen, R. L., Bernstein, G. M., & Malhotra, R. 2001, ApJL, 549, L241
Astropy Collaboration 2013, A&A, 558, A33
Astropy Collaboration 2018, AJ, 156, 123
Banda-Huarca, M. V., Camargo, J. I. B., Desmars, J., et al. 2019, AJ, 157, 120
Bannister, M. T., Gladman, B. J., Kavelaars, J. J., et al. 2018, ApJS, 236, 18
Bannister, M. T., Kavelaars, J. J., Petit, J.-M., et al. 2016, AJ, 152, 70
Bannister, M. T., Shankman, C., Volk, K., et al. 2017, AJ, 153, 262
Batygin, K., & Brown, M. E. 2016, AJ, 151, 22
Becker, J. C., Khain, T., Hamilton, S. J., et al. 2018, AJ, 156, 81
Bernstein, G., & Khushalani, B. 2000, AJ, 120, 3323
Bernstein, G. M., Abbott, T. M. C., Desai, S., et al. 2017a, PASP, 129, 114502
Bernstein, G. M., Armstrong, R., Plazas, A. A., et al. 2017b, PASP, 129, 074503
Bernstein, G. M., Trilling, D. E., Allen, R. L., et al. 2004, AJ, 128, 1364
Bernstein, J. P., Kessler, R., Kuhlmann, S., et al. 2012, ApJ, 753, 152
Bertin, E., & Arnouts, S. 1996, A&AS, 117, 393
Brasser, R., & Schwamb, M. E. 2015, MNRAS, 446, 3788
Brout, D., Sako, M., Scolnic, D., et al. 2019, ApJ, 874, 106
Brown, A. G. A., Vallenari, A., Prusti, T., et al. 2016, A&A, 595, A2
Brown, M. E. 2001, AJ, 121, 2804
Brown, M. E., Trujillo, C. A., & Rabinowitz, D. L. 2005, ApJL, 635, L97
Burke, D. L., Rykoff, E. S., Allam, S., et al. 2017, AJ, 155, 41
Carrasco Kind, M., Drlica-Wagner, A., Koziol, A., & Petravick, D. 2019, JOSS, 4, 1022
Chen, Y.-T., Lin, H.-W., Alexandersen, M., et al. 2018, PASJ, 70, S38
Dawson, R. I., & Murray-Clay, R. 2012, ApJ, 750, 43
Denneau, L., Jedicke, R., Grav, T., et al. 2013, PASP, 125, 357
Diehl, H. T., Neilsen, E., Gruendl, R., et al. 2016, Proc. SPIE, 9910, 99101D
Diehl, H. T., Neilsen, E., Gruendl, R. A., et al. 2018, Proc. SPIE, 10704, 107040D
Drlica-Wagner, A., Sevilla-Noarbe, I., Rykoff, E. S., et al. 2018, ApJS, 235, 33
Duncan, M. J., Brasser, R., Dones, L., & Levison, H. F. 2008, in The Solar System Beyond Neptune, ed. M. A. Barucci et al. (Tucson, AZ: Univ. Arizona Press), 315
Duncan, M. J., Levison, H. F., & Budd, S. M. 1995, AJ, 110, 3073
Elliot, J. L., Kern, S. D., Clancy, K. B., et al. 2005, AJ, 129, 1117
Fernández, J., & Ip, W.-H. 1984, Icar, 58, 109
Flaugher, B., Diehl, H. T., Honscheid, K., et al. 2015, AJ, 150, 150
Fraser, W. C., Brown, M. E., & Schwamb, M. E. 2010, Icar, 210, 944
Gaia Collaboration, Brown, A. G. A., Vallenari, A., et al. 2018, A&A, 616, A1
Gerdes, D. W., Jennings, R. J., Bernstein, G. M., et al. 2016, AJ, 151, 39
Gerdes, D. W., Sako, M., Hamilton, S., et al. 2017, ApJL, 839, L15
Gladman, B., Marsden, B. G., & Vanlaerhoven, C. 2008, in The Solar System Beyond Neptune, ed. M. A. Barucci et al. (Tucson, AZ: Univ. Arizona Press), 43
Gladman, B. J., Davis, D. R., Neese, C., et al. 2009, Icar, 202, 104
Goldstein, D. A., D'Andrea, C. B., Fischer, J. A., et al. 2015, AJ, 150, 82

Gomes, R. S. 2003, Icar, 161, 404

González, Á 2010, Math. Geosci., 42, 49

Guennebaud, G., Jacob, B., et al. 2010, Eigen v3, http://eigen.tuxfamily.org

Hahn, J. M., & Malhotra, R. 2005, AJ, 130, 2392

Holman, M. J., Payne, M. J., Blankley, P., Janssen, R., & Kuindersma, S. 2018, AJ, 156, 135

Hunter, J. D. 2007, CSE, 9, 90

Jarvis, M., Bernstein, G., & Jain, B. 2003, MNRAS, 352, 338

Jewitt, D., & Luu, J. 1993, Natur, 362, 730

Jílková, L., Portegies Zwart, S., Pijloo, T., & Hammer, M. 2015, MNRAS, 453, 3158

Jones, D. O., Scolnic, D. M., Riess, A. G., et al. 2018, ApJ, 857, 51

Jones, E., Oliphant, T., Peterson, P., et al. 2001, SciPy: Open Source Scientific Tools for Python, Version 1.3.2, http://www.scipy.org/

Jones, R. L., Gladman, B., Petit, J.-M., et al. 2006, Icar, 185, 508

Kaib, N. A., & Sheppard, S. S. 2016, AJ, 152, 133

Kessler, R., Brout, D., D'Andrea, C. B., et al. 2019, MNRAS, 485, 1171

Kessler, R., Marriner, J., Childress, M., et al. 2015, AJ, 150, 72

Khain, T., Becker, J. C., Adams, F. C., et al. 2018, AJ, 156, 273

Khain, T., Gerdes, D., Becker, J., Adams, F., et al. 2020, AJ, in press (arXiv:2001.06060)

Kubica, J., Denneau, L., Grav, T., et al. 2007, Icar, 189, 151

Levison, H. F., Morbidelli, A., VanLaerhoven, C., Gomes, R., & Tsiganis, K. 2008, Icar, 196, 258

Lin, H.-W., Chen, Y.-T., Wang, J.-H., et al. 2018, PASJ, 70, S39

Lin, H. W. W., Gerdes, D. J., Hamilton, S., et al. 2019, Icar, 321, 426

Lindegren, L., Lammers, U., Bastian, U., et al. 2016, A&A, 595, A4

Malhotra, R. 1993, Natur, 365, 819

Maneewongvatana, S., & Mount, D. M. 1999, arXiv:cs/9901013v1

Morbidelli, A., Levison, H. F., & Gomes, R. 2008, in The Solar System Beyond Neptune, ed. M. A. Barucci et al. (Tucson, AZ: Univ. Arizona Press), 275

Morganson, E., Gruendl, R. A., Menanteau, F., et al. 2018, PASP, 130, 074501

Neilsen, E., & Annis, J. 2013, ObsTac: Automated Execution of Dark Energy Survey Observing Tactics, http://lss.fnal.gov/archive/2013/conf/fermilab-conf-13-397-cd.pdf

Nesvorný, D. 2015, AJ, 150, 73

Nesvorný, D., & Vokrouhlický, D. 2016, ApJ, 825, 94

Ofek, E. O. 2012, ApJ, 749, 10

Oliphant, T. E. 2015, Guide to NumPy (2nd ed.; USA: CreateSpace)

Pence, W. 1999, in ASP Conf. Ser. 172, Astronomical Data Analysis Software and Systems VIII, ed. D. M. Mehringer, R. L. Plante, & D. A. Roberts (San Francisco, CA: ASP), 487

Perdelwitz, V., Völschow, M., & Müller, H. M. 2018, A&A, 615, A159

Pérez, F., & Granger, B. E. 2007, CSE, 9, 21

Petit, J.-M., Kavelaars, J. J., Gladman, B. J., et al. 2011, AJ, 142, 131

Pike, R. E., Fraser, W. C., Schwamb, M. E., et al. 2017, AJ, 154, 101

Rabinowitz, D., Schwamb, M. E., Hadjiyska, E., & Tourtellotte, S. 2012, AJ, 144, 140

Schwamb, M. E., Brown, M. E., Rabinowitz, D. L., & Ragozzine, D. 2010, ApJ, 720, 1691

Sheppard, S. S., & Trujillo, C. 2016, AJ, 152, 221

Sheppard, S. S., Trujillo, C., & Tholen, D. J. 2016, ApJL, 825, L13

Sheppard, S. S., Trujillo, C. A., Tholen, D. J., & Kaib, N. 2019, AJ, 157, 139

Sheppard, S. S., Williams, G. V., Tholen, D. J., et al. 2018, RNAAS, 2, 155

Stephens, D. C., & Noll, K. S. 2006, AJ, 131, 1142

Suchyta, E., Huff, E. M., Aleksić, J., et al. 2016, MNRAS, 457, 786

The Dark Energy Survey Collaboration 2018a, PhRv, D98, 043526

The Dark Energy Survey Collaboration 2018b, MNRAS, 480, 3879

The Dark Energy Survey Collaboration 2019a, MNRAS, 483, 4866

The Dark Energy Survey Collaboration 2019b, ApJL, 872, L30

The Dark Energy Survey Collaboration 2019c, PhRvL, 122, 171301

Tombaugh, C. W. 1946, ASPL, 5, 73

Trujillo, C. A., Jewitt, D. C., & Luu, J. X. 2001, AJ, 122, 457

Trujillo, C. A., & Sheppard, S. S. 2014, Natur, 507, 471

Tsiganis, K., Gomes, R., Morbidelli, A., & Levison, H. F. 2005, Natur, 435, 459

Volk, K., & Malhotra, R. 2017, AJ, 154, 62

Weryk, R. J., Lilly, E., Chastel, S., et al. 2016, arXiv:1607.04895